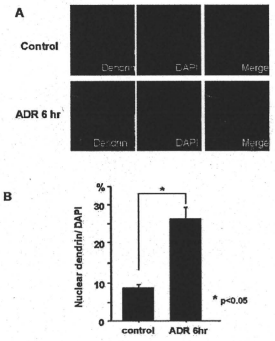

Figure 5

170x245mm (220 x 220 DPI)

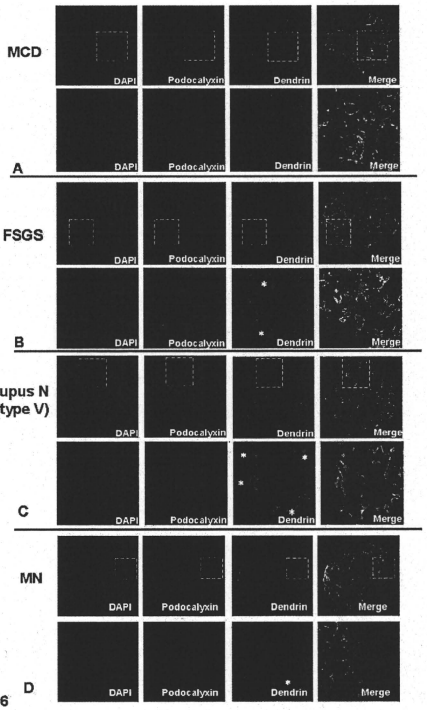

Figure 6

170x245mm (143 x 143 DPI)

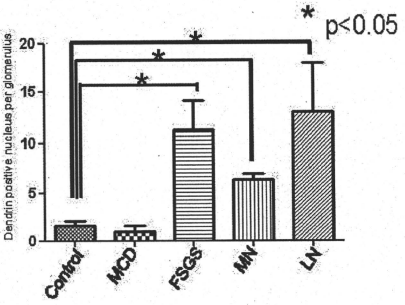

Figure 7

170x245mm (73 x 77 DPI)

DRUG DELIVERY

Improving Drug Potency and Efficacy by Nanocarrier-Mediated Subcellular Targeting

Mami Murakami,[1] Horacio Cabral,[1,2] Yu Matsumoto,[3] Shourong Wu,[3] Mitsunobu R. Kano,[4] Takao Yamori,[5] Nobuhiro Nishiyama,[2,3]* Kazunori Kataoka[1,2,3,6]*

Nanocarrier-mediated drug targeting is an emerging strategy for cancer therapy and is being used, for example, with chemotherapeutic agents for ovarian cancer. Nanocarriers are selectively accumulated in tumors as a result of their enhanced permeability and retention of macromolecules, thereby enhancing the antitumor activity of the nanocarrier-associated drugs. We investigated the real-time subcellular fate of polymeric micelles incorporating (1,2-diaminocyclohexane) platinum(II) (DACHPt/m), the parent complex of oxaliplatin, in tumor tissues by fluorescence-based assessment of their kinetic stability. These observations revealed that DACHPt/m was extravasated from blood vessels to the tumor tissue and dissociated inside each cell. Furthermore, DACHPt/m selectively dissociated within late endosomes, enhancing drug delivery to the nearby nucleus relative to free oxaliplatin, likely by circumvention of the cytoplasmic detoxification systems such as metallothionein and methionine synthase. Thus, these drug-loaded micelles exhibited higher antitumor activity than did oxaliplatin alone, even against oxaliplatin-resistant tumors. These findings suggest that nanocarriers targeting subcellular compartments may have considerable benefits in clinical applications.

INTRODUCTION

In 2009, about 10 million people worldwide were newly diagnosed with cancer (*1*). Application of nanotechnology to cancer therapy may offer therapeutic effects that cannot be achieved with other strategies. The main aim of this approach is to develop nanoscale drug vehicles for targeted cancer therapy (*2–5*). Nanocarriers selectively accumulate in solid tumors as a result of the enhanced permeability and retention (EPR) effect, which is characterized by microvascular hyperpermeability to circulating macromolecules and impaired lymphatic drainage in tumor tissues (*6*). At present, several nanocarrier formulations have been approved for clinical use against ovarian cancer and HIV-associated Kaposi's sarcoma (Doxil) and breast cancer (Abraxane). These formulations allow better accumulation of the drugs doxorubicin and paclitaxel in tumors (*7*).

Polymeric micelles, self-assemblies of block copolymers, have gained increasing popularity as tumor-targetable nanocarriers since they were first used as drug vehicles in the late 1980s (*8–12*). These micelles, which are several tens of nanometers in size and have a characteristic core-shell structure consisting of a drug-loaded hydrophobic core and poly(ethylene glycol) (PEG) hydrophilic shell, are long-lived in the bloodstream and effectively accumulate in solid tumors after intravenous injection (*8*). The critical features of polymeric micelles for their function as drug vehicles, including size, drug loading and release, and specific binding to the target cells, can be modulated by engineering the constituent block copolymers. At present, our micelle formulations incorporating doxorubicin, paclitaxel, SN-38, cisplatin, and (1,2-diaminocyclohexane) platinum(II) (DACHPt) are undergoing clinical trials (development code names NK911, NK105, NK012, NC-6004, and NC-4016, respectively), and four of these have advanced to Phase II studies (*13–17*). These clinical studies have revealed that polymeric micelles reduce side effects from the incorporated drugs and are effective against various intractable tumors, such as triple-negative breast cancers (*18*), indicating their clinical potential.

Recently, increasing attention has been paid to another potentially useful property of nanocarriers: to achieve subcellular drug targeting. Subcellular drug targeting of nanocarriers could enhance the pharmacological activity of the loaded drugs through improved subcellular drug distribution (*19*). Drug vehicles designed to release active drugs in acidic organelles, such as the endosome and lysosome, can circumvent recognition by the drug efflux pump (for example, P-glycoprotein) through internalization by endocytosis, thus overcoming multidrug resistance in cancer cells (*20–22*). Here, we aimed to investigate the potential of DACHPt-loaded micelles (DACHPt/m) for in vivo subcellular targeting. DACHPt/m is formed by the polymer-metal complexation between DACHPt and the carboxylic group of poly(ethylene glycol)-*b*-poly(glutamic acid) [PEG-*b*-P(Glu)] copolymers. DACHPt is the parent complex of the clinically approved drug oxaliplatin. Oxaliplatin has a hydrolyzable oxalate group to increase its solubility in water, which can be removed by nucleophiles in biological media, such as chloride ions. Aqua complexes ($[(DACH)Pt(H_2O)Cl]^+$ or $[(DACH)Pt(H_2O)_2]^{2+}$) of DACHPt exhibit chemotherapeutic activity. DACHPt/m releases DACHPt and the micelle structure dissociates depending on the pH and chloride ion concentrations, a result of ligand substitution of the Pt(II) from the carboxylates in the micelle core with the chloride ions in the medium (Fig. 1A) (*23*, *24*). Moreover, after DACHPt/m is internalized into cancer cells, it would be expected to be exposed to different pH and chloride ion concentrations during subcellular trafficking (*25*). We hypothesized that DACHPt/m would be selectively released in low-pH cellular compartments, bypassing

[1]Department of Bioengineering, Graduate School of Engineering, University of Tokyo, 7-3-1 Hongo, Bunkyo-ku, Tokyo 113-8656, Japan. [2]Center for NanoBio Integration, University of Tokyo, Tokyo 113-8656, Japan. [3]Center for Disease Biology and Integrative Medicine, Graduate School of Medicine, University of Tokyo, Tokyo 113-0033, Japan. [4]Department of Molecular Pathology, Graduate School of Medicine, University of Tokyo, Tokyo 113-0033, Japan. [5]Division of Molecular Pharmacology, Cancer Chemotherapy Center, Japanese Foundation for Cancer Research, 3-10-6 Ariake, Koto-ku, Tokyo 135-8550, Japan. [6]Department of Materials Engineering, Graduate School of Engineering, University of Tokyo, Tokyo 113-8656, Japan.
*To whom correspondence should be addressed. E-mail: nishiyama@bmw.t.u-tokyo.ac.jp (N.N.); kataoka@bmw.t.u-tokyo.ac.jp (K.K.)

cytoplasmic detoxification and thereby improving potency and efficacy (Fig. 1B). Indeed, we previously reported that cisplatin-loaded micelles, which are formed in the same manner as DACHPt/m, caused different gene expression patterns than did cisplatin alone because of their different internalization pathways and the facilitated drug release in endosomes and lysosomes (*26*). To test the above-mentioned hypothesis, we constructed fluorescent-labeled DACHPt/m (F-DACHPt/m) with a dual fluorescent-labeling method so that we could follow the intracellular localization and dissociation of the micelles by using in vivo confocal microscopy, and intravitally evaluated the extravasation, penetration, cellular uptake, and subcellular fate of DACHPt/m in tumor tissues and their activity against human colorectal cancers.

RESULTS

Construction and characterization of F-DACHPt/m

To construct the dual fluorescent-labeled block copolymer, we conjugated the fluorescent dyes boron dipyrromethene (BODIPY) FL (excitation wavelength, 503 nm; emission wavelength, 512 nm) and BODIPY TR (excitation wavelength, 588 nm; emission wavelength, 616 nm) to the α- and ω-end groups of α-4-(diethoxymethyl)benzyl-poly(ethylene glycol)-*b*-poly(L-glutamic acid), respectively, and thus obtained BODIPY FL-PEG-*b*-P(Glu)-BODIPY TR (fig. S1). The conjugation degree for BODIPY FL to the block copolymer was 0.2 mol BODIPY FL per mole of polymer and for BODIPY TR was about 0.8 mol BODIPY TR per mole of polymer. We built F-DACHPt/m by the formation of polymer-metal complexes between DACHPt and the carboxylic groups of poly(glutamic acid) in BODIPY FL-PEG-*b*-P(Glu)-BODIPY TR (Fig. 1A). F-DACHPt/m had a diameter of 30 nm, similar to that of DACHPt/m (fig. S2). The intact F-DACHPt/m emitted fluorescence only from the shell-conjugated dye (BODIPY FL) because the core-conjugated dye (BODIPY TR) was quenched owing to its high local concentration. The close proximity of BODIPY TR fluorophores in the core of the micelles leads to self-quenching by the formation of nonfluorescent ground-state BODIPY TR dimers (or higher aggregates) (*27*). When DACHPt is released as a result of the ligand substitution of the Pt(II) from the carboxylates in the micelle core with the chloride in the medium, the density of the micelle core is reduced and the fluorescence of BODIPY TR is dequenched (Fig. 1A). We investigated the release of DACHPt from F-DACHPt/m and the fluorescence of BODIPY FL and BODIPY TR at the surface and core of the micelles, respectively, under conditions that mimicked the extracellular medium (pH 7.4 and 150 mM Cl^-), early endosomes (pH 6.9 and 20 mM Cl^-), and late endosomes and lysosomes (pH 5.5 and 70 mM Cl^-) (*25*). The fluorescence from BODIPY FL on the shell of the micelles was constant regardless of the pH and salt concentration of the media (Fig. 2, A to C, middle columns), suggesting that the fluorescence from BODIPY FL can be used to trace the position of the micelles in the biological environment. In addition, the drug release profile of F-DACHPt/m was similar to that of unmodified DACHPt/m, suggesting the feasibility of a direct comparison (Fig. 2, A to C, left columns). Under extracellular conditions, BODIPY TR fluorescence increased after an incubation period of 17 hours, simultaneous with the release of DACHPt from F-DACHPt/m (Fig. 2A). The release of DACHPt from F-DACHPt/m in the late endosomal conditions was considerably faster (Fig. 2C) than in the extra-

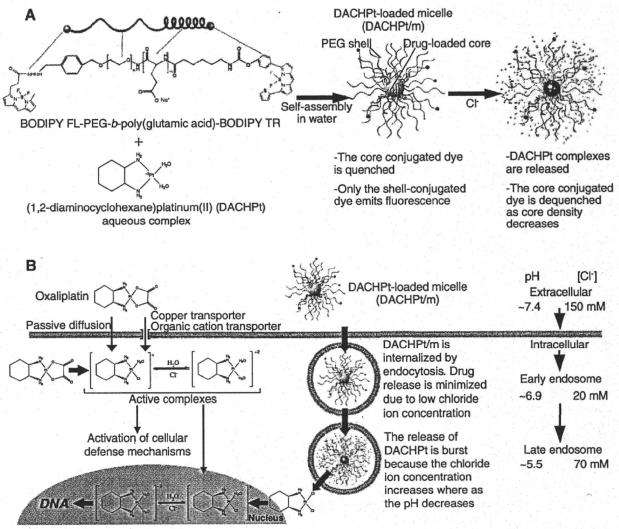

Fig. 1. Design of fluorescent-labeled DACHPt/m (F-DACHPt/m) for visualization of the localization and drug release in the cell. **(A)** F-DACHPt/m self-assembled through polymer-metal complex formation between DACHPt and boron dipyrromethene (BODIPY) FL–poly(ethylene glycol)-*b*-poly(glutamic acid)–BODIPY TR in distilled water. In the micelle state, only BODIPY FL (green) emits fluorescence, whereas BODIPY TR (red) remains quenched. As DACHPt is released from F-DACHPt/m in chloride ion–containing media, BODIPY TR is dequenched and emits fluorescence. **(B)** Schematic representation of hypothetical subcellular pathways and action of DACHPt/m. Oxaliplatin enter cells by passive diffusion or through copper/organic cation transporters. Once oxaliplatin is in the cytoplasm, most of the activated aqua species ($[(DACH)Pt(H_2O)Cl]^+$ or $[(DACH)Pt(H_2O)_2]^{2+}$) are eliminated by cellular detoxification mechanisms, but a small fraction binds to DNA. In contrast, DACHPt/m that enters tumor cells by endocytosis (middle) is exposed to an environment with increasing acidity and chloride ion concentration because early endosomes mature into the late endosomes. Drug release from DACHPt/m is accelerated in the late endosomal environment close to the perinuclear region, resulting in enhanced efficiency of drug delivery to the nucleus.

cellular and early endosomal conditions (Fig. 2, A and B), occurring without any delay. Further, mirroring the DACHPt release, F-DACHPt/m exhibited more robust fluorescence recovery of BODIPY TR under the late endosomal conditions (Fig. 2C) than under the early endosomal conditions (Fig. 2B, right columns). Thus, the fluorescence profiles of BODIPY TR are correlated with the release profiles of DACHPt from the micelles.

In vitro subcellular trafficking of F-DACHPt/m

The cellular internalization and fate of F-DACHPt/m in human tumor-derived colorectal cancer (HT29) cells, which are the most frequently used cell lines in oxaliplatin studies (*28*), were observed with time-lapse confocal laser scanning microscopy (CLSM) (Fig. 3A and video S1). The intensity of BODIPY FL fluorescence increased slightly over time (Fig. 3B), and the BODIPY FL fluorescence in the images was clearly visible within a 6-hour incubation (Fig. 3A). Meanwhile, with time, the intensity of BODIPY TR fluorescence continuously increased to a greater extent than did that of BODIPY FL fluorescence (Fig. 3B), and the BODIPY TR fluorescence in the images became visible at about 24 hours of incubation (Fig. 3A). This continuous increase in the intensity of BODIPY TR fluorescence corresponds to the dequenching of BODIPY TR fluorescence driven by the release of DACHPt in the cell. These results suggest that F-DACHPt/m enters the cells as a micelle form and then dissociates within the subcellular environments.

Using CLSM with higher magnification, we further evaluated the detailed subcellular trafficking and fate of F-DACHPt/m by focusing on individual cells. We confirmed that the micelles entered the cancer cells via endocytosis by incubating the cells with F-DACHPt/m at 37°C and 4°C. As endocytosis ceases at 4°C, the fluorescent signal of F-DACHPt/m inside the cells was undetectable, whereas at 37°C, the fluorescence from F-DACHPt/m was observed inside the cells (fig. S3). To examine the subcellular trafficking of the micelles, we determined the colocalization of BODIPY FL fluorescence from F-DACHPt/m with an early endosome marker, Rab5a-RFP, and a late endosome and lysosome marker, LysoTracker, in HT29 cells (Fig. 3C). Note that individual vesicular organelles can be recognized as punctate fluorescence in the images. After a 6-hour incubation at 37°C, BODIPY FL colocalized mainly with Rab5a-RFP (yellow fluorescence in Fig. 3C, upper images) rather than with LysoTracker. After prolonged incubation (24 and 55 hours), BODIPY FL showed decreased colocalization with Rab5a-RFP and increased colocalization with LysoTracker (yellow fluorescence in Fig. 3C, lower images). This observation was confirmed by quantification of colocalized fluorescent intensities of BODIPY FL with Rab5a-RFP or LysoTracker (Fig. 3D). These results suggested that the micelles might localize mainly in the early endosome until 6 hours and then move into the late endosome/lysosome compartment. Furthermore, we studied the timing and location of the micelle dissociation and concomitant drug release by evaluating the colocalization of F-DACHPt/m with LysoTracker (Fig. 3E and fig. S4A) and the quantification of BODIPY FL and BODIPY TR fluorescent intensities (fig. S4B), as well as the colocalization ratio (Fig. 3F). The fluorescence intensity from BODIPY FL gradually increased (fig. S4B). Meanwhile, the fluorescence of BODIPY TR became visible after 24-hour incubation (Fig. 3E and fig. S4A) and then increased over time (fig. S4B). Both BODIPY FL and BODIPY TR colocalized with LysoTracker (Fig. 3E and fig. S4A), and the colocalization ratio between BODIPY FL or BODIPY TR and LysoTracker increased over time (Fig. 3F). These observations sug-

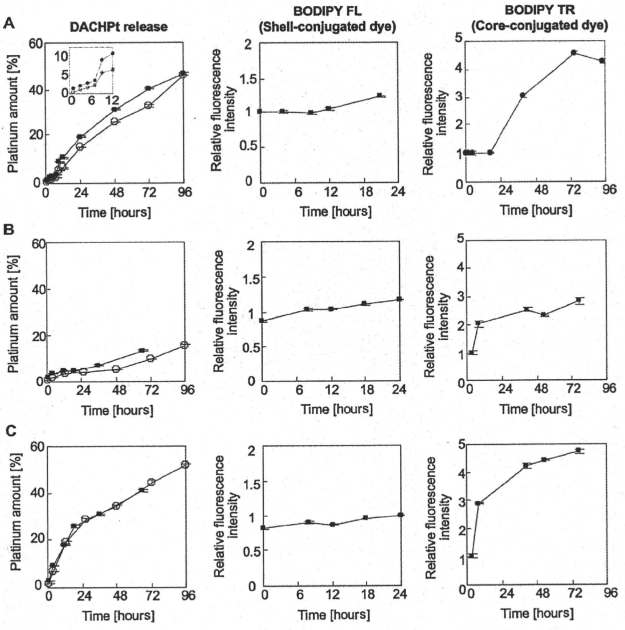

Fig. 2. Properties of F-DACHPt/m under conditions mimicking extracellular and subcellular environments. (**A** to **C**) Release profiles of DACHPt from DACHPt/m and F-DACHPt/m (left column) and fluorescence profiles of BODIPY FL (middle column) and BODIPY TR (right column) under conditions mimicking (A) the extracellular environment (10 mM PBS, pH 7.4, and 150 mM NaCl), (B) the early endosomal environment (10 mM PBS, pH 6.9, and 20 mM NaCl), and (C) the late endosomal environment (10 mM PBS, pH 5.5, and 70 mM NaCl), all at 37°C. Inset in top left panel is the magnification of the profiles of DACHPt release until 12 hours. The release of DACHPt from the micelles was evaluated by dialysis as described in Materials and Methods. Data for DACHPt/m and F-DACHPt/m in the left column are shown as open and filled circles, respectively. Data are expressed as means ± SEM ($n = 3$).

gested that F-DACHPt/m progressively dissociated in the late endosome and lysosomal compartments. Because these acidic organelles reside in the perinuclear region, F-DACHPt/m would be expected to deliver the active platinum complexes close to the nucleus. Thus, in vitro confocal microscopy revealed that F-DACHPt/m appears to exhibit late endosome/lysosome–selective dissociation concomitant with the release of DACHPt, thereby achieving efficient DACHPt delivery close to the nucleus.

Effect of subcellular pathway on drug efficiency

Oxaliplatin enters the cells by passive diffusion or through copper/organic cation transporters (*29*), and it then changes to active DACHPt aqua complexes in the cytoplasm, some of which may ultimately cross-link with DNA, disrupting DNA function and exerting therapeutic activity (Fig. 1B). However, 75 to 85% of activated platinum drugs are sequestered by abundant sulfur species that serve as cellular defense mechanisms in the cytoplasm, and only 5 to 10% of oxaliplatin can bind to DNA (Fig. 1B) (*30*–*32*). We hypothesized that DACHPt/m facilitates drug delivery close to the nucleus through its perinuclear subcellular localization. Therefore, we studied the pharmacological activity of DACHPt/m. DACHPt/m displayed a value of IC_{50} (the mean concentration that causes 50% growth inhibition) against HT29 cells that was lower than that of oxaliplatin by a factor of 4.7 (Table 1). It is rare that a nanocarrier-encapsulated drug surpasses the free form of the drug for in vitro cytotoxicity (*33*). To elucidate the mechanism of DACHPt/m action, we evaluated the subcellular accumulation of platinum and quantity of Pt-DNA adducts. Exposure of HT29 cells to oxaliplatin resulted in twice as much accumulation of platinum than did exposure to DACHPt/m (Fig. 3G). This is probably because oxaliplatin rapidly enters the cells by diffusion and through copper/organic cation transporters (*29*), whereas DACHPt/m is gradually internalized by endocytosis. Nevertheless, we did not observe a significant difference in the Pt-DNA adducts formed after exposure to oxaliplatin and DACHPt/m (Fig. 3H), indicating that DACHPt/m may efficiently deliver the active platinum drug to DNA (Fig. 3I).

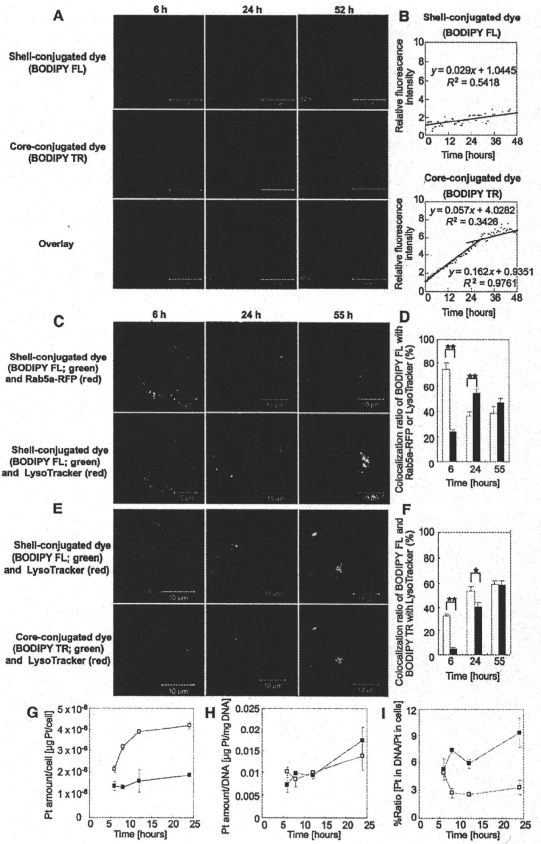

Fig. 3. In vitro observation of subcellular trafficking and fate of F-DACHPt/m, cellular platinum accumulation, and formation of platinum-DNA adducts. (**A**) Representative images of time-lapse CLSM observation of HT29 cells treated with F-DACHPt/m (green, BODIPY FL; red, BODIPY TR; yellow, their colocalization). (**B**) Relative fluorescence intensity of BODIPY FL (upper) and BODIPY TR (lower) of F-DACHPt/m. (**C**) Fluorescent images of colocalization of BODIPY FL of DACHPt/m (green) with an early endosome marker, Rab5a-RFP (red in upper images), or a late endosome and lysosome marker, LysoTracker (red in lower images), in HT29 cells after incubation for 6, 24, and 55 hours. (**D**) Colocalization ratio of BODIPY FL with Rab5a-RFP (open bars) or LysoTracker (closed bars). Data are expressed as means ± SEM ($n = 10$). $^{**}P < 0.01$. (**E**) Fluorescent images of colocalization of BODIPY FL (green in upper images) and BODIPY TR (green in lower images) of F-DACHPt/m with LysoTracker (red) in HT29 cells after incubation for 6, 24, and 55 hours. (**F**) Colocalization ratio of BODIPY FL (open bars) or BODIPY TR (closed bars) with LysoTracker. Data are expressed as means ± SEM ($n = 10$). $^{*}P < 0.05$; $^{**}P < 0.01$. (**G**) In vitro cellular accumulation of platinum. (**H**) DNA platination. (**I**) Ratio of platinum in DNA to total platinum in cells expressed as a percentage. DNA platination was converted from μg Pt/mg DNA to μg Pt/cell, and the ratio was calculated. Open squares, oxaliplatin; filled squares, DACHPt/m. Data are expressed as means ± SEM ($n = 3$).

We also evaluated the mean concentration required for 50% growth inhibition (GI_{50}), which is defined as in (*34*, *35*), in a human cell panel composed of 37 cancer cell lines (fig. S5), and investigated the correlation between GI_{50} and expression of 26 genes that we selected on the basis of their potential association with the pharmacological activity of platinum compounds (*36*). The cytotoxic activity of oxaliplatin was inversely correlated with the expression of metallothionein (MT1Q) and methionine synthase (MTR), which are found in the cytoplasm and inactivate platinum compounds. DACHPt/m cytotoxicity did not exhibit similar correlations (table S1). We conclude that DACHPt/m may bypass cytoplasmic detoxification by MTR and MT1Q and efficiently deliver active platinum complexes to the nucleus, because they are internalized by endocytosis and selectively release the active platinum complexes in the late endosome/lysosome compartment (Fig. 1B).

Effect of DACHPt/m on oxaliplatin resistance in vitro

Our proposed mechanism of action of DACHPt/m led us to investigate their efficacy in oxaliplatin-resistant cancer cells, because MTR and MT1Q are overexpressed in these cells (*37*–*39*). We developed oxaliplatin-resistant HT29 cells (HT29/ox) by chronic exposure of HT29 cells to oxaliplatin with gradual dose escalation. Relative to the parental HT29 cells, HT29/ox cells were 10 times as resistant to oxaliplatin (Table 1). Quantitative real-time reverse transcription polymerase chain reaction (RT-PCR) and Western blotting revealed that the HT29/ox cells showed up-regulated messenger RNA (mRNA) as well as protein for MTR and MT1Q compared with HT29 cells (Fig. 4, A and B). Moreover, the down-regulation of MT1Q and MTR with small interfering RNA (siRNA) restored the sensitivity of HT29/ox cells to oxaliplatin (fig. S6). In vitro cytotoxicity studies showed that DACHPt/m was 120 times as cytotoxic as oxaliplatin in HT29/ox cells (Table 1). These results suggested that DACHPt/m may overcome acquired resistance to oxaliplatin.

In vivo intratumoral imaging of F-DACHPt/m in a human colon cancer model

DACHPt/m would need to extravasate, penetrate into the interstitial tissue, and be internalized by cancer cells after systemic administration to exert the in vivo antitumor activity predicted from the results above. We performed real-time intravital observation of the accumulation and subcellular fate of F-DACHPt/m in HT29 xenografts by using in vivo CLSM equipped with a high-speed resonant scanner developed to acquire live tissue images of experimental animals (fig. S7). Immediately after intravenous injection, F-DACHPt/m was observed in the blood vessels of solid tumors (Fig. 5A and video S2). The fluorescence from F-DACHPt/m in the blood vessels corresponded only to that of BODIPY FL. Even 12 hours later, only BODIPY FL fluorescence was observed flowing in the blood vessels (Fig. 5B and video S3). These observations indicate that F-DACHPt/m stably circulates in the bloodstream while maintaining their micellar structure. Images of tumor tissue revealed the accumulation and dissociation behaviors of F-DACHPt/m (Fig. 5, C and D, and video S3). Two hours after injection, F-DACHPt/m accumulated within the tumor tissue because of the EPR effect and was identified within the cells, whereas BODIPY TR fluorescence remained quenched. BODIPY TR fluorescence gradually appeared inside the cells 4 hours after injection and was clearly visible after 12 hours, indicating the release of DACHPt

Table 1. In vitro cytotoxicity of free oxaliplatin and DACHPt/m against HT29 and HT29/ox cells after a 48-hour incubation. Data are expressed as means ± SEM (n = 4).

Cells	IC_{50} (μM)*		
	Free oxaliplatin	DACHPt/m	Oxaliplatin/DACHPt/m
HT29	2.2 ± 2.2	0.47 ± 0.05	4.7
HT29/ox	22.8 ± 2.6	0.19 ± 0.11	120
Ratio of HT29/ox/HT29	10.4	0.4	—

*IC_{50} values obtained from the MTT assay.

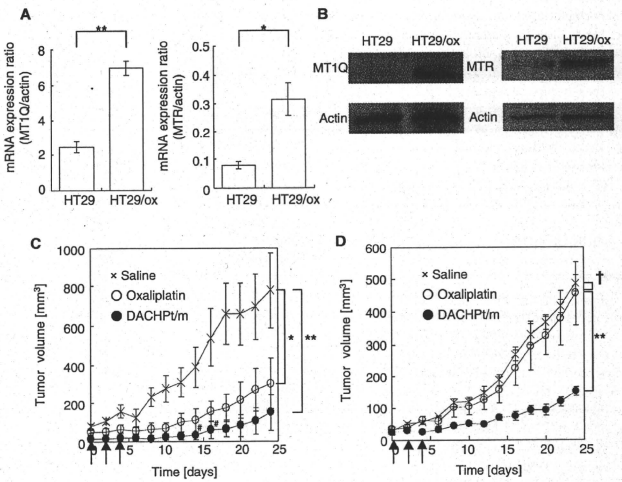

Fig. 4. Expression of MT1Q and MTR in HT29/ox cells and effects of DACHPt/m on HT29 and HT29/ox tumors in vivo. (**A**) Relative mRNA expression of metallothionein (MT1Q) and methionine synthase (MTR) in parent HT29 and HT29/ox cell lines. Data are expressed as means ± SEM (n = 3). *P < 0.05; **P < 0.01. (**B**) Western blots of MT1Q and MTR in HT29 and HT29/ox cell lines. (**C** and **D**) In vivo effect of DACHPt/m on subcutaneous HT29 (C) and HT29/ox (D) tumor cells. Crosses, saline; open circles, oxaliplatin (8 mg/kg); filled circles, DACHPt/m (4 mg/kg); arrows, injection of oxaliplatin and DACHPt/m; #, tumor regression; †P > 0.1; *P < 0.05; **P < 0.01. Data are expressed as means ± SEM (n = 4).

from the micelles inside the cells in the tumor tissue. The cell membrane, stained with CellMask, and cell nuclei were substantially free of F-DACHPt/m (Fig. 5, C and D, and video S3). These results were consistent with our in vitro results (Fig. 3A) and suggested that F-DACHPt/m percolated into interstitial tissues and was efficiently internalized to endosomal compartments of cells in a micelle form, followed by dissociation of the multimolecular structure of the micelles in the late endosomal and lysosomal compartments.

DACHPt/m enhances antitumor activity and overcomes oxaliplatin resistance in vivo

On the basis of our observations of the in vivo behavior of F-DACHPt/m, we hypothesized that DACHPt/m may also overcome oxaliplatin resistance in vivo. Thus, we evaluated DACHPt/m in vivo antitumor activity against subcutaneous HT29 and HT29/ox tumors (Fig. 4, C and D). Although free oxaliplatin failed to inhibit the growth of HT29/ox tumors, DACHPt/m exhibited substantial antitumor activity in the oxaliplatin-resistant xenograft model and successfully overcame the oxaliplatin resistance of HT29/ox cells in vivo (Fig. 4D). Note that DACHPt/m also achieved higher antitumor activity than oxaliplatin against the HT29 tumors (Fig. 4C). Thus, our micelle-based drug delivery vehicle was able to circumvent the detoxification mechanisms against platinum drugs in tumor cell cytoplasm through selective subcellular drug release and hence overcome acquired resistance.

DISCUSSION

Colorectal cancer is a major cause of morbidity and mortality worldwide (*1*). Oxaliplatin is currently the standard therapy for colorectal cancer, and acquired resistance to oxaliplatin is a major clinical drawback in the treatment of colorectal cancer [virtually all metastatic colorectal cancer becomes resistant to oxaliplatin, with a median time to progression of 8.7 months (*40*)]. The major cellular processes by which oxaliplatin enters and attacks cancer cells include uptake and transport, formation of DNA adducts and their recognition by damage response proteins, and signal transduction leading to apoptosis. Any factors that interfere with these pathways can lead to drug resistance (*41*). Here, we showed that DACHPt/m can overcome drug resistance by circumventing recognition by MTR and MT1Q, and achieve subcellular drug delivery both in vitro and in vivo to the perinuclear region of cells. It has been reported that drug delivery systems can overcome multidrug resistance

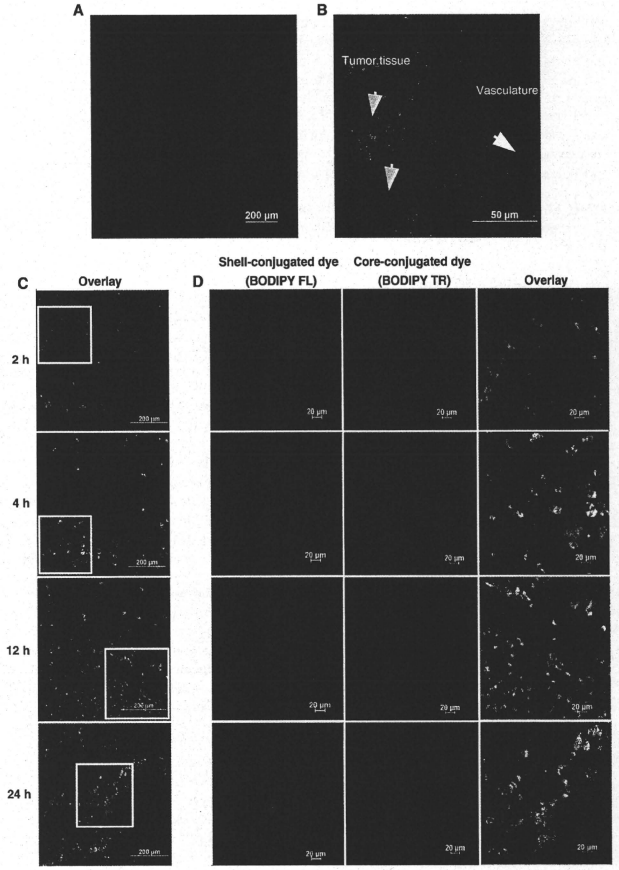

Fig. 5. In vivo CLSM observation of F-DACHPt/m in blood vessels and tumors after intravenous administration. (**A** and **B**) CLSM observation of F-DACHPt/m in the blood vessels of solid tumors (A) immediately after injection and (B) in the tumor tissue at 12 hours after injection. Yellow arrows, tumor tissue; white arrow, blood vessel. (**C**) Time-dependent CLSM observation of F-DACHPt/m in the tumor tissues at 2, 4, 12, and 24 hours after injection. Green, fluorescence from the shell-conjugated dyes (BODIPY FL); red, core-conjugated dyes (BODIPY TR); blue, cell surfaces stained by CellMask. (**D**) Magnification of selected areas [square regions in (C)] by channel.

by avoiding the drug efflux mechanism of P-glycoprotein (*20*–*22*). Because P-glycoprotein is not associated with platinum drug resistance (*42*), we used a different approach. Our data indicate that cytoplasmic detoxification mechanisms against platinum drugs can potentially be avoided by using the appropriate drug delivery system.

Nanocarriers encounter numerous barriers in vivo en route to their target during the processes of blood circulation, extravasation, penetration, and cellular uptake. It is therefore difficult to extrapolate in vivo outcomes of a drug-nanocarrier combination from its in vitro behavior, although real-time observation of in vivo behaviors such as we have used here can ascertain critical barriers residing in a living body and facilitate the design of a nanocarrier optimized for in vivo delivery. The in vivo CLSM technique that we used in this study enabled spatiotemporal and quantitative analyses of extravasation, tissue penetration, and cellular internalization of nanocarriers in living animals. Using dual fluorescent labeling of DACHPt/m, we elucidated the real-time intratumoral behavior of DACHPt/m. The dual fluorescent label of DACHPt micelles allowed us to trace the micelles' position by the ever-present fluorescent signal from the surface of the micelles, and the drug release and dissociation of the multimolecular structure of the micelles by the dequenching and fluorescence recovery of the core-conjugated dye. In in vitro cellular experiments, these micelles were internalized intact, and then they were disassembled and the drug was released in late endosomes. In our in vivo microscopy, we observed that DACHPt/m maintained their micelle form during circulation in the blood, probably because of the stable inner core structure formed by the polymer-metal complexes, and extravasated into solid tumors. DACHPt/m was able to deeply penetrate cancerous tissue after extravasation and was internalized by different cell populations that were distant from the blood vessels. Such efficient penetration of tissue is a requirement of successful drug delivery and a prerequisite for effective subcellular targeting. It has been reported that PEG-modified liposomes with 100-nm diameter accumulated at perivascular regions of solid tumors and failed to penetrate the tumor interstitium deeply (*43*). Although this characteristic may depend on the cancer type, it is possible that the deep tumor penetration of DACHPt/m is a result of their smaller 30-nm size. Finally, the DACHPt/m structure dissociated at the perinuclear regions of the cell after internalization, based on the pH and chloride ion concentration–selective release of DACHPt. This observation is also consistent with our hypothesis that DACHPt/m can overcome oxaliplatin resistance in tumors by bypassing the cytoplasmic detoxification mechanisms of MTR and MT1Q. There are, however, several limitations to the type of study that we have performed in a subcutaneous tumor model. Compared with subcutaneous tumors, orthotopic and spontaneously forming tumors may have characteristic differences such as vascular density and degree of fibrosis, which may affect the transport of nanocarriers (*44*).

Our research provides one approach for subcellular targeting of cytoplasmic drugs. Such nanocarriers have the potential to enhance the drug efficacy and overcome drug resistance.

MATERIALS AND METHODS

Materials

γ-Benzyl L-glutamate and bis(trichloromethyl) carbonate (triphosgene) were purchased from Sigma Chemical and Tokyo Kasei Kogyo, respectively. *N*,*N*-Dimethylformamide (DMF), 3-(4,5-dimethylthiazol-2-yl)-2,5-diphenyltetrazolium bromide (MTT), and dimethyl sulfoxide (DMSO) were purchased from Wako Pure Chemicals. Oxaliplatin and $NaCH_3CN$ were purchased from Sigma-Aldrich Inc. Dichloro(1,2-diammino cyclohexane) platinum(II) was purchased from W. C. Heraeus GmbH. α-Methoxy-ω-amino-poly(ethylene glycol) [CH_3O-PEG-NH_2; molecular weight (MW), 12,000] was purchased from Nippon Oil and Fats. BODIPY TR-succinimidyl ester, BODIPY FL-hydrazide, LysoTracker Blue, CellLight Early Endosome-RFP (Rab5a-RFP), CellMask, and Lipofectamine RNAiMAX were purchased from Invitrogen.

Cell lines and animals

HT29 cells were purchased from the American Type Culture Collection. HT29 cells were maintained in McCoy's 5A modified medium (Invitrogen) containing 10% fetal bovine serum (Gibco) as well as 1% penicillin and streptomycin (Sigma) and were cultured at 37°C in a humidified atmosphere of 5% CO_2. To develop HT29/ox cells (*45*), we treated HT29 cells with oxaliplatin at IC_{50} doses for 1 hour. After 24 hours, cells were subcultured into new flasks and oxaliplatin was added to a culture of 80% confluent cells. The concentration was incrementally increased by factors of 1.2 to 2. The process was continued until the cells were resistant to drug concentrations at least 10 times as great. BALB/c-nu/nu mice (female; body weight, 18 to 20 g; age, 6 weeks old) were purchased from Charles River Japan. All animal experiments were carried out in accordance with the guidelines for animal experiments at the University of Tokyo, Japan.

Methods

Synthesis of block copolymers. α-4-(Diethoxymethyl)benzyl-ω-amino-poly(ethylene glycol) (Ac-Bz-PEG-NH_2) was previously synthesized in our laboratory (*46*). Poly(ethylene glycol)-*b*-poly(L-glutamic acid) [PEG-*b*-P(Glu)] [MW_{PEG}, 12,000; polymerization degree of P(Glu), 20] and Ac-Bz-PEG-*b*-poly(L-glutamic acid) [Ac-Bz-PEG-*b*-P(Glu)] [MW_{PEG}, 12,000; polymerization degree of P(Glu), 20] were synthesized according to the previously described synthetic method (*47*). Briefly, *N*-carboxyanhydride of γ-benzyl L-glutamate (BLG-NCA) was synthesized by the Fuchs-Farthing method with triphosgene (*48*). BLG-NCA was polymerized in DMF initiated by the amino group of CH_3O-PEG-NH_2 or Ac-Bz-PEG-NH_2 to obtain PEG-*b*-poly(γ-benzyl L-glutamate) (PEG-*b*-PBLG) or Ac-Bz-PEG-*b*-PBLG, respectively. The MW distribution of PEG-*b*-PBLG and Ac-Bz-PEG-*b*-PBLG was determined by gel permeation chromatography (GPC) [column, TSK-gel G3000HHR, G4000HHR (Tosoh); eluent, DMF containing 10 mM LiCl; flow rate, 0.8 ml/min; detector, refractive index; temperature, 25°C]. PEG-*b*-PBLG and Ac-Bz-PEG-*b*-PBLG showed narrow MW distributions (M_w/M_n: 1.09 and 1.16, respectively) in GPC. The degrees of polymerization of PBLG in PEG-*b*-PBLG and Ac-Bz-PEG-*b*-PBLG were determined to be 20 by comparing the proton ratios of methylene units in PEG (-OCH_2CH_2-: δ = 3.7 ppm) and phenyl groups of PBLG (-$CH_2C_6H_5$: δ = 7.3 ppm) in ^{1}H-NMR (nuclear magnetic resonance) measurement. Both PEG-*b*-PBLG and Ac-Bz-PEG-*b*-PBLG were deprotected by mixing with 0.5 N NaOH at room temperature to obtain PEG-*b*-P(Glu) and Ac-Bz-PEG-*b*-P(Glu), respectively. Complete deprotection was confirmed by ^{1}H NMR measurement.

Preparation of micelles. For conjugation of BODIPY TR to a polymer, a solution of BODIPY TR-succinimidyl ester in DMSO (1 mg/ml) was mixed with Ac-Bz-PEG-*b*-P(Glu). The reaction was carried out overnight at room temperature with stirring. Unreacted

BODIPY TR was removed by dialysis [MW cutoff (MWCO) size, 2000 daltons] against DMSO and water. To conjugate BODIPY FL to the Ac-Bz-PEG-*b*-P(Glu)-BODIPY TR polymer, we mixed a solution of BODIPY FL-hydrazide in DMSO with the polymer, followed by the addition of 1 N HCl to deprotect the acetal group. Samples were stirred overnight at room temperature and treated with $NaBH_3CN$ to reduce the link between BODIPY FL and the polymer. For purification, unbound BODIPY FL was removed by dialysis (MWCO, 2000 daltons) against DMSO and water. The prepared BODIPY FL-PEG-*b*-P(Glu)-BODIPY TR copolymer was freeze-dried overnight and stored at −20°C. DACHPt/m and F-DACHPt/m were prepared according to the previously described method (*23*). DACHPt (5 mM) was suspended in distilled water and mixed with silver nitrate ([$AgNO_3$]/[DACHPt] = 1) to form aqueous complexes. The solution was kept in the dark at 25°C for 24 hours. AgCl precipitates were eliminated by centrifugation. The supernatant was purified by passage through a 0.22-μm filter. DACHPt aqueous complex solution was then mixed with PEG-*b*-P(Glu) or BODIPY FL-PEG-*b*-P(Glu)-BODIPY TR ([Glu] = 5 mM; [DACHPt]/[Glu] = 1.0) and reacted for 120 hours to obtain DACHPt/m or F-DACHPt/m, respectively. DACHPt/m and F-DACHPt/m were purified by ultrafiltration (MWCO, 30,000 daltons; Fig. 1A). The size distributions of DACHPt/m and F-DACHPt/m were evaluated by dynamic light scattering at 25°C with a Zetasizer Nano ZS90 (Malvern Instruments). The platinum content of DACHPt/m was determined by ion-coupled plasma mass spectrometry (4500 ICP-MS; Hewlett Packard).

Drug release and fluorescence profiles of micelles under different conditions. The release of platinum from DACHPt/m and F-DACHPt/m in phosphate-buffered saline (PBS) at 37°C was evaluated as described (*23*). Briefly, a micelle solution of known platinum concentration was placed inside a dialysis bag (MWCO, 2000 daltons). The solution was then dialyzed against PBS under different conditions mimicking the extracellular environment (10 mM PBS, pH 7.4, and 150 mM NaCl), early endosomes (10 mM PBS, pH 6.9, and 20 mM NaCl), and late endosomes (10 mM PBS, pH 5.5, and 70 mM NaCl) at 37°C (*25*). The concentration of platinum present in the dialysate was determined with ICP-MS. The fluorescence profiles of F-DACHPt/m were also evaluated under the same conditions with a spectrofluorometer (FP6600, Jasco) or NanoDrop (ND3300, Scrum). Changes in fluorescence intensity were measured at a defined time period.

In vitro observation of subcellular localization and the fate of F-DACHPt/m by CLSM. HT29 cells were cultured at 1×10^5 cells in 35-mm glass-based dishes (Asahi Techno Glass). After overnight incubation in a fresh medium, the cells were washed twice with PBS. The medium was then replaced by 1 ml of fresh medium containing F-DACHPt/m (100 μM on Pt base). Live-cell CLSM imaging was performed with a Zeiss LSM 510 META nonlinear optics scan head attached to an inverted Axiovert 200 M SP equipped with a 63 × 1.4 numerical aperture Plan Apochromat oil immersion objective (Carl Zeiss). For long-term time-lapse imaging, culture dishes were wrapped with an optically clear foil cover (Carl Zeiss) to avoid evaporation and mounted onto the microscope stage incubator (37°C, 5% CO_2, 90% relative humidity). Bright-field DIC (differential interference contrast) images and fluorescent sequences were taken every 30 min for 72 hours. BODIPY FL was excited at 488 nm with an Ar laser and fluorescence was detected at 500 to 530 nm, whereas BODIPY TR was excited at 543 nm with a He-Ne laser, and fluorescence was detected at 565 to 615 nm. Laser power was kept low at 0.36 mW for 488 nm and at 0.018 mW for 543 nm so that photobleaching was negligible. To determine whether DACHPt/m was taken up by endocytosis, we treated HT29 cells with F-DACHPt/m at 37°C or 4°C for 6 hours and then observed by CLSM. For the colocalization studies, we used micelles prepared from BODIPY FL-PEG-P(Glu) that only emit fluorescence from the shell. HT29 cells, which had been preincubated with CellLight Early Endosome-RFP to express an early endosome marker, Rab5a-RFP, were treated with BODIPY FL–conjugated DACHPt/m, and images were taken at indicated time points after staining with LysoTracker Blue. Rab5a-RFP was excited at 543 nm with a He-Ne laser, and fluorescence was detected at 565 to 615 nm. LysoTracker Blue was excited in multiphoton mode at 710 nm with a Mai Tai tunable broadband laser (Spectra-Physics), and fluorescence was detected at 390 to 465 nm. Colocalization was quantified as follows:

$$\text{amount of colocalization (\%)} = \text{BODIPY FL pixels}_{\text{colocalization}}/\text{BODIPY FL pixels}_{\text{total}} \times 100$$

where BODIPY FL $\text{pixels}_{\text{colocalization}}$ represents the number of BODIPY FL pixels colocalizing with Rab5a-RFP or LysoTracker pixels in the cytoplasm, and BODIPY FL $\text{pixels}_{\text{total}}$ represents the number of all BODIPY FL pixels in the cytoplasm. The timing and location of the micelle dissociation and concomitant drug release were studied by evaluating the colocalization of BODIPY FL and BODIPY TR signals from F-DACHPt/m with the late endosomes/lysosomes (Fig. 3, E and F). Cells were treated with F-DACHPt/m, and images were taken at indicated time points after staining with LysoTracker Blue. Colocalization was quantified as follows:

$$\text{amount of colocalization (\%)} = \text{BODIPY FL or BODIPY TR pixels}_{\text{colocalization}}/\text{BODIPY FL or BODIPY TR pixels}_{\text{total}} \times 100$$

where BODIPY FL or BODIPY TR $\text{pixels}_{\text{colocalization}}$ represents the number of BODIPY FL or BODIPY TR pixels colocalizing with LysoTracker pixels in the cytoplasm, and BODIPY FL or BODIPY TR $\text{pixels}_{\text{total}}$ represents the number of all BODIPY FL or BODIPY TR pixels in the cytoplasm.

Determination of subcellular Pt accumulation and amount of Pt-DNA adducts. HT29 cells (6×10^6) were seeded in 100-mm tissue culture dishes. After 24 hours, cells were treated with 10 μM oxaliplatin or DACHPt/m on a platinum base. After 6, 8, 12, and 24 hours of drug exposure, the medium was removed and the cells were washed three times with PBS, scraped, and harvested. Samples were freeze-dried overnight, dissolved in heated nitric acid, and evaporated to dryness. The samples were redissolved in water and the Pt content was determined by ICP-MS. For the quantification of Pt-DNA adducts, DNA was extracted with a DNA purification kit (Promega) according to the manufacturer's protocol. The amount and purity of DNA were determined by measuring absorption at 260 and 280 nm with NanoDrop (ND3300). The DNA was dissolved in nitric acid, dried, and redissolved in water. The Pt content was determined by ICP-MS, and the DNA platination levels were expressed as micrograms of Pt per milligram of DNA.

In vitro cytotoxicity study against human cancer cells. The in vitro cytotoxicity of oxaliplatin and DACHPt/m was examined against a panel of 37 human cancer cells as described (*34*, *35*). Cancer cells were plated into flat-bottomed 96-well plates at 5×10^3 per well. Cells were treated by continuous exposure to oxaliplatin or DACHPt/m in a final volume of 100 μl. Plates were incubated for 48 hours at 37°C in a humidified atmosphere with 5% CO_2, and cell viability was determined

by MTT assay. To determine the relationship between cellular sensitivity to oxaliplatin or DACHPt/m and the expression of genes involved in the sensitivity or resistance of cells to platinum compounds, we assessed the gene expression profile of 21 human cancer cell lines for 26 genes selected on the basis of previous studies on cisplatin- or oxaliplatin-resistant cells (*36*). Expression of these individual genes was determined by searching the National Cancer Institute database. The coefficient of correlation between the GI_{50}s of free oxaliplatin and DACHPt/m as well as the level of gene expression was calculated for each gene.

Quantitative real-time RT-PCR. The expression of the metallothionein (MT1Q) [human MT1B (same as MT1Q), NM_005947, 4MQ-012725-01-0002] and methionine synthase (MTR) (human MTR, NM_000254, 4LQ-009896-00-0002) was confirmed by quantitative real-time RT-PCR. After 24 hours of treatment, cells were washed with PBS and harvested. Total RNA was prepared with TRIzol (Invitrogen), and complementary DNA (cDNA) was reverse-transcribed with a QuantiTect reverse transcription kit (Qiagen). PCR primer sequences were as follows: MT1Q, 5′-GAACTCCAGGCTTGTCTTGG-3′ (forward) and 5′-CATTTGCACTCTTTGCACTTG-3′ (reverse); MTR, 5′-ACCCAACTTCCAGGGAGACT-3′ (forward) and 5′-GGCAC-CATGATCTTGGACTT-3′ (reverse); actin, 5′-AGATGTGGATCAG-CAAGCAG-3′ (forward) and 5′-GCGCAAGTTAGGTTTTGTCA-3′ (reverse); and 18*S*, 5′-CGGCGACGACCCATTCGAAC-3′ (forward) and 5′-GAATCGAACCCTGATTCCCCGTC-3′ (reverse). cDNA from HT29 cells was amplified with specific primers with a SYBR Green Core Reagent Kit (Qiagen) and a real-time PCR instrument (Applied Biosystems). Expression of each gene was standardized with endogenous actin or 18*S* as a control, and its relative levels in HT29 or HT29/ox cells were quantified by calculating $2^{-\Delta\Delta C_T}$, where $\Delta\Delta C_T$ is the difference in C_T (cycle number at which the amount of amplified target reaches a fixed threshold) between target and reference.

MT1Q and MTR gene knockdown. The siRNAs against MT1Q and MTR and the control siRNA were purchased from Thermo Fisher Scientific Inc. The siRNA target sequences against MT1Q are the following: siMT1Q, GCAAAGGCUCAUCAGAGAA. The siRNA sequences against MTR are the following: siMTR, CUGAGAAGCU-CUUACGUUA. The siRNAs were transfected into the cell with Lipofectamine RNAiMAX (Invitrogen) according to the instructions of the manufacturer. Briefly, HT29/ox cells (4×10^5) were seeded in six-well plates. Twenty-four hours later, the mixture of siMT1Q (50 nM) and siMTR (50 nM) was transfected into the cells with Lipofectamine RNAiMAX reagent. Knockdown of MT1Q and MTR was separately confirmed by real-time PCR (fig. S6, A and B, respectively). To investigate the role of MT1Q and MTR in the oxaliplatin resistance in HT29/ox cells, we seeded HT29/ox cells (5×10^3) in 96-well plates, and 24 hours later, the mixture of siMT1Q (50 nM) and siMTR (50 nM) or the control siRNA was transfected into the cells with Lipofectamine RNAiMAX reagent. Twenty-four hours after transfection, the transfected HT29/ox cells were treated by continuous exposure to oxaliplatin in a final volume of 100 μl. Plates were further incubated for 48 hours at 37°C in a humidified atmosphere with 5% CO_2, and their cytotoxicity was determined by MTT assay.

Western blotting. HT29 or HT29/ox cells (5×10^6) were seeded in 100-mm^2 plates and washed with PBS (100 μl). Cell extracts were resolved in TNE buffer [1% NP-40, 150 mM NaCl, 10 mM tris-HCl, 1 mM EDTA, aprotinin (10 μg/ml), 2 mM Na_3VO_4, 10 mM NaF]. The cell suspension was centrifuged for 20 min at 15,000*g*. Sampling buffer (4×) was added to the aliquots, followed by incubation for 5 min at 100°C. Transfer to a polyvinylidene difluoride membrane (Invitrogen) was performed by electrophoresis for 90 min at 125 V. Membranes were blocked with 6% nonfat milk or tris-buffered saline (TBS) with 0.1% Tween 20 (MT1Q) for 1 hour. They were then probed at room temperature with the following antibodies: anti-metallothionein (ab12228, 1:1000, Abcam), anti–methionine synthase (ab66039, 1:2000, Abcam), and anti–β-actin (#4967, 1:1000, Cell Signaling). Membranes were washed three times with washing buffer (TBS with 0.1% Tween 20) and then probed with the secondary anti–rabbit immunoglobulin G (IgG) horseradish peroxidase (HRP) (W401B, 1:10,000, Promega) or anti–mouse IgG HRP (W402B, 1:10,000, Promega) conjugate for 1 hour. The secondary antibody was washed three times with washing buffer and then evenly coated with enhanced chemiluminescence (ECL) Western blotting detection reagents (GE Healthcare) for 30 s. The membrane was immediately exposed to Fuji Medical X-ray film (Fujifilm) at room temperature for various periods in a film cassette. Protein levels were standardized with the signal from the β-actin probe.

In vivo antitumor activity studies. BALB/c-nu/nu mice (female, $n = 4$) were inoculated subcutaneously with HT29 or HT29/ox cells (1×10^7/ml). Tumors were allowed to grow for 1 week (tumor size at this point was about 40 mm^3). Mice were then treated intravenously three times at 2-day intervals with oxaliplatin (8 mg/kg) or DACHPt/m (4 mg/kg) on a platinum base. Antitumor activity was evaluated in terms of tumor size (V) with the following equation:

$$V = a \times b^2/2$$

Here, a and b are the major and minor axes, respectively, of the tumor as measured by a caliper.

Intravital observation of the in vivo behavior of F-DACHPt/m. Intravital observation of F-DACHPt/m was performed as described (*49*). Female BALB/c mice (6 to 8 weeks old) were inoculated subcutaneously with HT29 cells (1×10^7/ml). After 5 days, when the tumor volumes reached 70 mm^3, F-DACHPt/m (10 mg/kg) was administered intravenously. At 2, 4, 12, and 24 hours after treatment, mice were anesthetized with 2.5% isoflurane (Abbott Japan) with a Univentor 400 Anesthesia Unit (Univentor). An arc-shaped incision was made around the subcutaneous tumor, and the skin flap was elevated without injuring the feeding vessels. The mouse was placed directly onto a thermoplate (Tokai Hit), and the skin flap was everted and stretched with several bent 30-gauge needles. The plasma membrane stain, CellMask Deep Red, was directly applied to the subcutaneous tumor, and a coverslip (Muto Pure Chemicals) was attached with just enough pressure to flatten the tumor surface. All in vivo images were acquired with a Nikon A1R CLSM attached to an upright Eclipse FN1 (Nikon). The A1R incorporates a conventional galvano scanner and a high-speed resonant scanner. The latter allows an acquisition speed of 30 frames per second while maintaining a relatively high resolution of 512 × 512 scanned points. BODIPY FL, BODIPY TR, and CellMask were excited with three lasers (488-nm Ar, 560-nm He-Ne, and 640-nm He-Ne lasers), and the fluorescent signals were detected. Laser powers were kept at 19.5 mW for 488-nm Ar, 7.5 mW for 561-nm He-Ne, and 1 mW for 640-nm He-Ne.

Statistical analysis. Data are presented as means ± SEM. The significant differences between the groups were analyzed by a Student's t test, and a P value of <0.05 was considered significant.

SUPPLEMENTARY MATERIAL

www.sciencetranslationalmedicine.org/cgi/content/full/3/64/64ra2/DC1

Fig. S1. Synthetic scheme of BODIPY FL-PEG-*b*-P(Glu)-BODIPY TR.

Fig. S2. Size distribution of DACHPt/m and F-DACHPt/m as determined by dynamic light scattering.

Fig. S3. Fluorescent images of HT29 cells after 6-hour incubation with F-DACHPt/m at 37°C and 4°C.

Fig. S4. In vitro CLSM observation of dissociation of F-DACHPt/m in the late endosomes/lysosomes.

Fig. S5. In vitro cytotoxicity of oxaliplatin and DACHPt/m against a human cancer cell panel.

Fig. S6. Knockdown of MT1Q and MTR restores the sensitivity of HT29/ox to oxaliplatin.

Fig. S7. Schematic illustration of experimental settings of in vivo CLSM.

Table S1. Coefficient of correlation between the GI_{50}s of free oxaliplatin or DACHPt/m and the expression levels of genes involved in the sensitivity or resistance of cells to platinum compounds.

Video S1. In vitro live imaging.

Video S2. In vivo live imaging (immediately after injection).

Video S3. In vivo live imaging (12 hours after injection).

REFERENCES AND NOTES

1. A. Jemal, R. Siegel, E. Ward, Y. Hao, J. Xu, M. J. Thun, Cancer statistics, 2009. *CA Cancer J. Clin.* **59**, 225–249 (2009).
2. T. M. Allen, P. R. Cullis, Drug delivery systems: Entering the mainstream. *Science* **303**, 1818–1822 (2004).
3. M. Ferrari, Cancer nanotechnology: Opportunities and challenges. *Nat. Rev. Cancer* **5**, 161–171 (2005).
4. V. P. Torchilin, Recent advances with liposomes as pharmaceutical carriers. *Nat. Rev. Drug Discov.* **4**, 145–160 (2005).
5. R. Duncan, The dawning era of polymer therapeutics. *Nat. Rev. Drug Discov.* **2**, 347–360 (2003).
6. Y. Matsumura, H. Maeda, A new concept for macromolecular therapeutics in cancer chemotherapy: Mechanism of tumoritropic accumulation of proteins and the antitumor agent Smancs. *Cancer Res.* **46**, 6387–6392 (1986).
7. M. E. Davis, Z. G. Chen, D. M. Shin, Nanoparticle therapeutics: An emerging treatment modality for cancer. *Nat. Rev. Drug Discov.* **7**, 771–782 (2008).
8. N. Nishiyama, K. Kataoka, Current state, achievements, and future prospects of polymeric micelles as nanocarriers for drug and gene delivery. *Pharmacol. Ther.* **112**, 630–648 (2006).
9. M. Yokoyama, M. Miyauchi, N. Yamada, T. Okano, Y. Sakurai, K. Kataoka, S. Inoue, Characterization and anticancer activity of the micelle-forming polymeric anticancer drug adriamycin-conjugated poly(ethylene glycol)-poly(aspartic acid) block copolymer. *Cancer Res.* **50**, 1693–1700 (1990).
10. K. Kataoka, G. S. Kwon, M. Yokoyama, T. Okano, Y. Sakurai, Block copolymer micelles as vehicles for drug delivery. *J. Control. Release* **24**, 119–132 (1993).
11. K. Kataoka, A. Harada, Y. Nagasaki, Block copolymer micelles for drug delivery: Design, characterization and biological significance. *Adv. Drug Deliv. Rev.* **47**, 113–131 (2001).
12. A. V. Kabanov, E. V. Batrakova, D. W. Miller, Pluronic block copolymers as modulators of drug efflux transporter activity in the blood–brain barrier. *Adv. Drug Deliv. Rev.* **55**, 151–164 (2003).
13. Y. Matsumura, K. Kataoka, Preclinical and clinical studies of anticancer agent-incorporating polymer micelles. *Cancer Sci.* **100**, 572–579 (2009).
14. Y. Matsumura, T. Hamaguchi, T. Ura, K. Muro, Y. Yamada, Y. Shimada, K. Shirao, T. Okusaka, H. Ueno, M. Ikeda, N. Watanabe, Phase I clinical trial and pharmacokinetic evaluation of NK911, a micelle-encapsulated doxorubicin. *Br. J. Cancer* **91**, 1775–1781 (2004).
15. T. Hamaguchi, K. Kato, H. Yasui, C. Morizane, M. Ikeda, H. Ueno, K. Muro, Y. Yamada, T. Okusaka, K. Shirao, Y. Shimada, H. Nakahama, Y. Matsumura, A phase I and pharmacokinetic study of NK105, a paclitaxel-incorporating micellar nanoparticle formulation. *Br. J. Cancer* **97**, 170–176 (2007).
16. T. Hamaguchi, T. Doi, T. Eguchi-Nakajima, K. Kato, Y. Yamada, Y. Shimada, N. Fuse, A. Ohtsu, S. Matsumoto, M. Takanashi, Y. Matsumura, Phase I study of NK012, a novel SN-38–incorporating micellar nanoparticle, in adult patients with solid tumors. *Clin. Cancer Res.* **16**, 5058–5066 (2010).
17. R. H. Wilson, R. Plummer, J. Adam, M. M. Eatock, A. V. Boddy, M. Griffin, R. Miller, Y. Matsumura, T. Shimizu, H. Calvert, Phase I and pharmacokinetic study of NC-6004, a new platinum entity of cisplatin-conjugated polymer forming micelles. *J. Clin. Oncol.* **26**, 2573 (2008).
18. R. Dent, M. Trudeau, K. I. Pritchard, W. M. Hanna, H. K. Kahn, C. A. Sawka, L. A. Lickley, E. Rawlinson, P. Sun, S. A. Narod, Triple-negative breast cancer: Clinical features and patterns of recurrence. *Clin. Cancer Res.* **13**, 4429–4434 (2007).
19. J. A. Hubbell, Materials science. Enhancing drug function. *Science* **300**, 595–596 (2003).
20. T. Minko, P. Kopeckova, J. Kopecek, Efficacy of the chemotherapeutic action of HPMA copolymer-bound doxorubicin in a solid tumor model of ovarian carcinoma. *Int. J. Cancer* **86**, 108–117 (2000).
21. D. Kim, E. S. Lee, K. T. Oh, Z. G. Gao, Y. H. Bae, Doxorubicin-loaded polymeric micelle overcomes multidrug resistance of cancer by double-targeting folate receptor and early endosomal pH. *Small* **4**, 2043–2050 (2008).
22. K. Cho, X. Wang, S. Nie, Z. G. Chen, D. M. Shin, Therapeutic nanoparticles for drug delivery in cancer. *Clin. Cancer Res.* **14**, 1310–1316 (2008).
23. H. Cabral, N. Nishiyama, S. Okazaki, H. Koyama, K. Kataoka, Preparation and biological properties of dichloro(1,2-diaminocyclohexane)platinum(II) (DACHPt)-loaded polymeric micelles. *J. Control. Release* **101**, 223–232 (2005).
24. H. Cabral, N. Nishiyama, K. Kataoka, Optimization of (1,2-diamino-cyclohexane)platinum(II)-loaded polymeric micelles directed to improved tumor targeting and enhanced antitumor activity. *J. Control. Release* **121**, 146–155 (2007).
25. N. D. Sonawane, J. R. Thiagarajah, A. S. Verkman, Chloride concentration in endosomes measured using a ratioable fluorescent Cl^- indicator: Evidence for chloride accumulation during acidification. *J. Biol. Chem.* **277**, 5506–5513 (2002).
26. N. Nishiyama, F. Koizumi, S. Okazaki, Y. Matsumura, K. Nishio, K. Kataoka, Differential gene expression profile between PC-14 cells treated with free cisplatin and cisplatin-incorporated polymeric micelles. *Bioconjug. Chem.* **14**, 449–457 (2003).
27. I. D. Johnson, H. C. Kang, R. P. Haugland, Fluorescent membrane probes incorporating dipyrrometheneboron difluoride fluorophores. *Anal. Biochem.* **198**, 228–237 (1991).
28. S. Arnould, I. Hennebelle, P. Canal, R. Bugat, S. Guichard, Cellular determinants of oxaliplatin sensitivity in colon cancer cell lines. *Eur. J. Cancer* **39**, 112–119 (2003).
29. L. Kelland, The resurgence of platinum-based cancer chemotherapy. *Nat. Rev. Cancer* **7**, 573–584 (2007).
30. E. Raymond, S. Faivre, S. Chaney, J. Woynarowski, E. Cvitkovic, Cellular and molecular pharmacology of oxaliplatin. *Mol. Cancer Ther.* **1**, 227–235 (2002).
31. F. R. Luo, T. Y. Yen, S. D. Wyrick, S. G. Chaney, High-performance liquid chromatographic separation of the biotransformation products of oxaliplatin. *J. Chromatogr. B Biomed. Sci. Appl.* **724**, 345–356 (1999).
32. F. R. Luo, S. D. Wyrick, S. G. Chaney, Biotransformations of oxaliplatin in rat blood in vitro. *J. Biochem. Mol. Toxicol.* **13**, 159–169 (1999).
33. R. Duncan, Polymer conjugates as anticancer nanomedicines. *Nat. Rev. Cancer* **6**, 688–701 (2006).
34. T. Yamori, A. Matsunaga, S. Sato, K. Yamazaki, A. Komi, K. Ishizu, I. Mita, H. Edatsugi, Y. Matsuba, K. Takezawa, O. Nakanishi, H. Kohno, Y. Nakajima, H. Komatsu, T. Andoh, T. Tsuruo, Potent antitumor activity of MS-247, a novel DNA minor groove binder, evaluated by an *in vitro* and *in vivo* human cancer cell line panel. *Cancer Res.* **59**, 4042–4049 (1999).
35. S. Yaguchi, Y. Fukui, I. Koshimizu, H. Yoshimi, T. Matsuno, H. Gouda, S. Hirono, K. Yamazaki, T. Yamori, Antitumor activity of ZSTK474, a new phosphatidylinositol 3-kinase inhibitor. *J. Natl. Cancer Inst.* **98**, 545–556 (2006).
36. A. Vekris, D. Meynard, M. C. Haaz, M. Bayssas, J. Bonnet, J. Robert, Molecular determinants of the cytotoxicity of platinum compounds: The contribution of *in silico* research. *Cancer Res.* **64**, 356–362 (2004).
37. S. L. Kelley, A. Basu, B. A. Teicher, M. P. Hacker, D. H. Hamer, J. S. Lazo, Overexpression of metallothionein confers resistance to anticancer drugs. *Science* **241**, 1813–1815 (1988).
38. J. Holford, P. J. Beale, F. E. Boxall, S. Y. Sharp, L. R. Kelland, Mechanisms of drug resistance to the platinum complex ZD0473 in ovarian cancer cell lines. *Eur. J. Cancer* **36**, 1984–1990 (2000).
39. P. M. Deegan, I. S. Pratt, M. P. Ryan, The nephrotoxicity, cytotoxicity and renal handling of a cisplatin-methionine complex in male Wistar rats. *Toxicology* **89**, 1–14 (1994).
40. R. M. Goldberg, D. J. Sargent, R. F. Morton, C. S. Fuchs, R. K. Ramanathan, S. K. Williamson, B. P. Findlay, H. C. Pitot, S. R. Alberts, A randomized controlled trial of fluorouracil plus leucovorin, irinotecan, and oxaliplatin combinations in patients with previously untreated metastatic colorectal cancer. *J. Clin. Oncol.* **22**, 23–30 (2004).
41. D. Wang, S. J. Lippard, Cellular processing of platinum anticancer drugs. *Nat. Rev. Drug Discov.* **4**, 307–320 (2005).
42. I. Pastan, M. M. Gottesman, K. Ueda, E. Lovelace, A. V. Rutherford, M. C. Willingham, A retrovirus carrying an *MDR1* cDNA confers multidrug resistance and polarized expression of P-glycoprotein in MDCK cells. *Proc. Natl. Acad. Sci. U.S.A.* **85**, 4486–4490 (1988).
43. R. K. Jain, Delivery of molecular and cellular medicine to solid tumors. *Adv. Drug Deliv. Rev.* **46**, 149–168 (2001).
44. Y. Saito, M. Yasunaga, J. Kuroda, Y. Koga, Y. Matsumura, Antitumour activity of NK012, SN-38-incorporating polymeric micelles, in hypovascular orthotopic pancreatic tumour. *Eur. J. Cancer* **46**, 650–658 (2010).
45. M. Mishima, G. Samimi, A. Kondo, X. Lin, S. B. Howell, The cellular pharmacology of oxaliplatin resistance. *Eur. J. Cancer* **38**, 1405–1412 (2002).

46. Y. Akiyama, Y. Nagasaki, K. Kataoka, Synthesis of heterotelechelic poly(ethylene glycol) derivatives having α-benzaldehyde and ω-pyridyl disulfide groups by ring opening polymerization of ethylene oxide using 4-(diethoxymethyl)benzyl alkoxide as a novel initiator. *Bioconjug. Chem.* **15**, 424–427 (2004).
47. N. Nishiyama, S. Okazaki, H. Cabral, M. Miyamoto, Y. Kato, Y. Sugiyama, K. Nishio, Y. Matsumura, K. Kataoka, Novel cisplatin-incorporated polymeric micelles can eradicate solid tumors in mice. *Cancer Res.* **63**, 8977–8983 (2003).
48. W. H. Daly, D. Poche, The preparation of N-carboxyanhydrides of α-amino acids using bis(trichloromethyl)carbonate. *Tetrahedron Lett.* **29**, 5859–5862 (1988).
49. Y. Matsumoto, T. Nomoto, H. Cabral, Y. Matsumoto, S. Watanabe, R. J. Christie, K. Miyata, M. Oba, T. Ogura, Y. Yamasaki, N. Nishiyama, T. Yamasoba, K. Kataoka, Direct and instantaneous observation of intravenously injected substances using intravital confocal micro-videography. *Biomed. Opt. Express* **1**, 1209–1216 (2010).
50. **Acknowledgments:** M.M. thanks J. Ghaugas for his support and suggestions for preparing the manuscript and S. Hiro for his help with in silico data analysis. **Funding:** This research was supported in part by Funding Program for World-Leading Innovative R&D on Science and Technology (FIRST Program) from the Japan Society for the Promotion of Science (JSPS) and the Core Research Program for Evolutional Science and Technology (CREST) from the Japan Science and Technology Agency (JST). **Author contributions:** M.M. and H.C. designed and performed the experiments, analyzed the results, and wrote the manuscript. Y.M. performed the imaging experiments. S.W. performed the siRNA knockdown studies. T.Y. conducted human cell panel analysis. M.R.K. edited the manuscript. N.N. supervised the project and wrote the manuscript. K.K. supervised the project and edited the manuscript. **Competing interests:** The authors declare that they have no competing interests.

Submitted 14 June 2010
Accepted 10 December 2010
Published 5 January 2011
10.1126/scitranslmed.3001385

Citation: M. Murakami, H. Cabral, Y. Matsumoto, S. Wu, M. R. Kano, T. Yamori, N. Nishiyama, K. Kataoka, Improving drug potency and efficacy by nanocarrier-mediated subcellular targeting. *Sci. Transl. Med.* **3**, 64ra2 (2011).

Integrated Systems and Technologies

Cancer Research

Visible Drug Delivery by Supramolecular Nanocarriers Directing to Single-Platformed Diagnosis and Therapy of Pancreatic Tumor Model

Sachiko Kaida[1,3,7], Horacio Cabral[1,3], Michiaki Kumagai[1], Akihiro Kishimura[2], Yasuko Terada[4], Masaki Sekino[5], Ichio Aoki[6], Nobuhiro Nishiyama[1,3], Toru Tani[7], and Kazunori Kataoka[1,2,3]

Abstract

Nanoparticle therapeutics are promising platforms for cancer therapy. However, it remains a formidable challenge to assess their distribution and clinical efficacy for therapeutic applications. Here, by using multifunctional polymeric micellar nanocarriers incorporating clinically approved gadolinium (Gd)–based magnetic resonance imaging contrast agents and platinum (Pt) anticancer drugs through reversible metal chelation of Pt, simultaneous imaging and therapy of an orthotopic animal model of intractable human pancreatic tumor was successfully performed without any serious toxicity. The strong tumor contrast enhancement achieved by the micelles correlated with the 24 times increase of r_1 of the Gd chelates, the highest for the formulations using clinically approved Gd chelates reported to date. From the microsynchrotron radiation X-ray fluorescence spectrometry scanning of the lesions, we confirmed that both the Gd chelates and Pt drugs delivered by the micelles selectively colocalized in the tumor interior. Our study provides new insights for the design of theranostic micelles with high contrast enhancement and site-specific clinical potential. *Cancer Res; 70(18); 7031–41. ©2010 AACR.*

Introduction

Recently, there has been explosive development of chemotherapeutic agents for cancer, but the efficacies of anticancer drugs are still insufficient particularly for the treatment of intractable tumors, including pancreatic cancer. Although the latest advances in molecular targeting agents have shown specific efficiency, the survival time of patients is often extended only slightly, even when these agents are used in combination with other anticancer drugs. Moreover, the use of such drugs typically results in various characteristic side effects, such as interstitial pneumonia for gefitinib (1), cardiotoxicity for trastuzumab (2, 3), and thrombosis for bevacizumab (4). Alternatives to developing these compounds and antibodies selective for cancer cells, with the aim of modulating drug distribution in the body to accomplish selective drug accumulation in the tumor site, are thus needed, and for this purpose, nanometric-scale vehicles or nanocarriers directing therapeutics to the tumor site are a key platform.

In the last decade, several kinds of nanoparticle therapeutics platforms, including liposomes, nanoparticles, and polymeric micelles, have been developed to selectively deliver drugs to tumor sites (5–12). These approaches have been used to improve the therapeutic efficacy and to reduce the side effects of drugs incorporated in delivery carriers (13, 14), and nanoparticle therapeutics such as Doxil (15) or Abraxane (16) are already in clinical use. The tumor targeting of these nanoparticle therapeutics is based on the enhanced permeability and retention (EPR) effect (in other words, the increased accumulation of high–molecular weight compounds, such as nanoparticles, in tumor tissue due to the high permeability of tumor blood vessels and the retention of these compounds because of the impaired lymphatic drainage at the cancer site; ref. 17). In the late 1980s, we developed one of the auspicious nanoparticle therapeutics, polymeric micelles, a self-assembly of amphiphilic block copolymers consisting of hydrophobic segments forming the drug-loaded core and water-soluble segments forming the biocompatible shell (11, 12). The main advantages of this system are the possibility of incorporating a variety of drugs, including hydrophobic substances, metal complexes, and charged macromolecules such as nucleic acids, as well as controlling their release properties by engineering and modifying the micelle-forming block copolymers. Moreover, polymeric micelles can be designed to be responsive to environmental changes and capable of target

Authors' Affiliations: [1]Center for Disease Biology and Integrative Medicine, Graduate School of Medicine, [2]Department of Materials Engineering, Graduate School of Engineering, and [3]Center for NanoBio Integration, The University of Tokyo, Tokyo, Japan; [4]Japan Synchrotron Radiation Research Institute, SPring-8, Hyogo, Japan; [5]Department of Advanced Energy, Graduate School of Frontier Sciences, The University of Tokyo, Chiba, Japan; [6]Molecular Imaging Center, National Institute of Radiological Sciences, Chiba, Japan; and [7]Department of Surgery, Shiga University of Medical Science, Shiga, Japan

Note: Supplementary data for this article are available at Cancer Research Online (http://cancerres.aacrjournals.org/).

Corresponding Author: Kazunori Kataoka, Department of Materials Engineering, Graduate School of Engineering, The University of Tokyo, 7-3-1 Hongo, Bunkyo-ku, Tokyo 113-8656, Japan. Phone: 81-3-5841-7138; Fax: 81-3-5841-7139; E-mail: kataoka@bmw.t.u-tokyo.ac.jp.

doi: 10.1158/0008-5472.CAN-10-0303

recognition. Our micelle formulations incorporating Adriamycin, paclitaxel, SN-38, cisplatin, and DACHPt (activated oxaliplatin; NK911, NK105, NK012, NC6004, and NC4016, respectively) are being examined in clinical studies, and four of these formulations have advanced to phase II studies (18–21). These clinical studies have revealed that polymeric micelles showed reduced side effects and high effectiveness against various intractable tumors, including triple-negative breast cancers that do not express the genes for estrogen receptor, progesterone receptor, and Her2/neu (22). Consequently, polymeric micelles have been considered one of the most promising drug delivery systems (DDS) in the field of cancer chemotherapy.

Although a crucial breakthrough in cancer treatment has been achieved using several micelles, the methods for estimating the distribution and effectiveness of the micelles are ineffective and inadequate. The precise monitoring of their distribution and early feedback on treatment efficacy would allow clinicians to anticipate the therapeutic process in each cancer patient and customize medicine for cancer therapy. Thus, it is imperative to directly assess the biodistribution of the micelles and their cargo as well as the magnitude of their accumulation at the cancer site. Consequently, the development of micelles with both imaging and therapeutic functions [theranostic (23) micelles] will permit visualization of the distribution of the micelles inside the body and tumor in a real-time manner, allowing optimization of the treatment protocol according to the unique characteristics of the malignancies in individual patients (24–26).

We developed theranostic core-shell polymeric micelles based on the self-assembly of block copolymers with both a magnetic resonance imaging (MRI) function and cancer therapeutic capacity. The micelles incorporate gadolinium–diethylenetriaminepentaacetic acid (Gd-DTPA), a widely used T_1-weighted MRI (T1W) contrast agent (27), and (1,2-diaminocyclohexane)platinum(II) (DACHPt), the parent complex of the potent anticancer drug oxaliplatin, in their core by reversible complexation between DACHPt, Gd-DTPA, and poly(ethylene glycol)-*b*-poly(glutamic acid) [PEG-*b*-P(Glu); Fig. 1]. Accordingly, both the DACHPt and Gd-DTPA complexes, which can be excreted from the kidney, thus avoiding toxicity from long-term accumulation inside the body, are released from the micelles in a sustained manner under physiologic conditions. Moreover, the longitudinal relaxivity (r_1) of the micelles (i.e., their ability as an MRI contrast agent) increased ~24 times compared with that of free

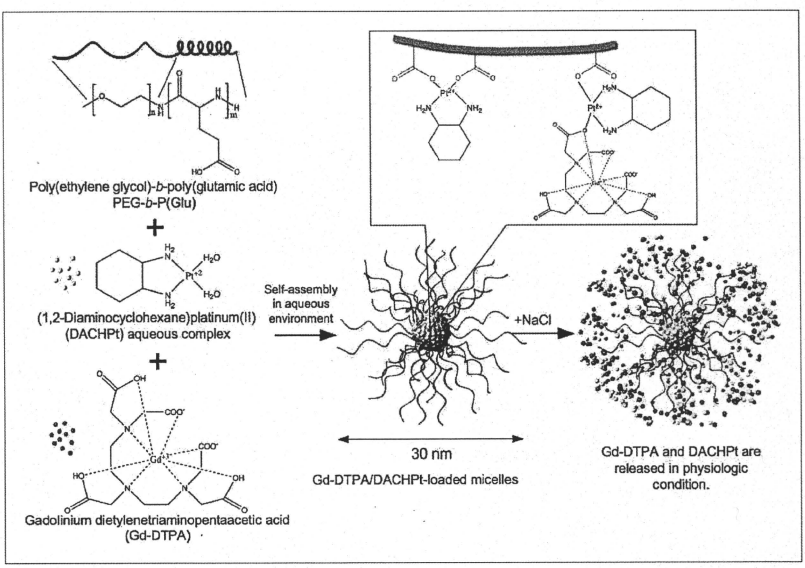

Figure 1. Schematic diagram of proposed self-assembly of Gd-DTPA/DACHPt–loaded micelles and release of Pt and Gd complexes from the micelles in chloride-containing medium.

Gd-DTPA, enabling, jointly with the enhanced tumor accumulation provided by the EPR effect, the improved detection of solid tumors. We also showed that the micelles have continuous and strong anticancer effect, and enhance the MRI contrast of the tumor region in an orthotopic human pancreatic cancer xenograft model much more intensely than Gd-DTPA alone, although the diagnosis and treatment of pancreatic cancer has been considered to be the most difficult among digestive cancers. Thus, the Gd-DTPA/DACHPt–loaded micelles are expected not only to improve the effectiveness and safety of the incorporated drugs but also to assist in the real-time monitoring of the drug distribution and tumor accumulation, suggesting the great potential of visible DDSs.

Materials and Methods

Cancer cell lines and animals

Murine colon adenocarcinoma 26 (C-26) cells were kindly supplied by the National Cancer Center. The BxPC3 human pancreatic adenocarcinoma cell line was obtained from the American Type Culture Collection. C-26 and BxPC3 cells were maintained in RPMI 1640 (Sigma-Aldrich, Inc.) containing 10% fetal bovine serum in a humidified atmosphere containing 5% CO_2 at 37°C. CDF_1 mice and BALB/c nude mice (female; 18–20 g body weight; 6 weeks old) were purchased from Charles River Japan. All animal experiments were carried out in accordance with the policies of the Animal Ethics Committee of the University of Tokyo.

Preparation of Gd-DTPA/DACHPt–loaded micelles

PEG-*b*-P(Glu) [Mw_{PEG} = 12,000 Da; polymerization degree of P(Glu) = 20] block copolymer was synthesized according to the previously described method (28). Briefly, the *N*-carboxy anhydride of γ-benzyl L-glutamate (Sigma Chemical) was synthesized by the Fuchs-Farthing method using triphosgene. Then, *N*-carboxy anhydride of γ-benzyl L-glutamate was polymerized in DMF initiated by the primary amino group of CH_3O-PEG-NH_2 (Nippon Oil and Fats) to obtain PEG-*b*-poly (γ-benzyl-L-glutamate) (PEG-*b*-PBLG). The polymerization degree was verified by comparing the proton ratios of methylene units in PEG (-OCH_2CH_2-: δ = 3.7 ppm) and phenyl groups of PBLG (-$CH_2C_6H_5$: δ = 7.3 ppm) in ^{1}H nuclear magnetic resonance (NMR) measurement (solvent: DMSO-d_6; JEOL EX270, JEOL, Inc.). PEG-*b*-PBLG was deprotected by mixing with 0.5 N NaOH at room temperature to obtain PEG-*b*-P(Glu). Complete deprotection was confirmed by ^{1}H-NMR measurement (solvent: D2O; temperature: 25°C).

Gd-DTPA (Aldrich Chemical) was converted to sodium salt by adjusting the pH to 7 with NaOH, and it was lyophilized. A 5 mmol/L solution of bis(nitrato) (*trans-l*-1,2-diaminocyclohexane)platinum(II) [DACHPt$(NO_3)_2$; W.C. Heraeus GmbH & Co. KG] in water was mixed with the sodium salt of Gd-DTPA (5 mmol/L), and the solution was maintained for 24 hours at 37°C. Then, PEG-*b*-P(Glu) ([Glu] = 5 mmol/L) was added to this solution ([DACHPt]/[Glu] = 1.0) and reacted for 120 hours at 37°C to prepare Gd-DTPA/DACHPt–loaded micelles. The micelles were purified by dialysis against distilled water [molecular weight cutoff size (MWCO): 2,000; Spectra/Por-6, Spectrum Laboratories] and by ultrafiltration (MWCO: 30,000). The size distribution of the Gd-DTPA/DACHPt–loaded micelles was evaluated by a dynamic light scattering (DLS) measurement at 25°C using a Zetasizer Nano ZS90 (Malvern Instruments). The Pt and Gd contents of the micelles were determined by inductively coupled plasma–mass spectrometry (ICP-MS; 4500 ICP-MS, Hewlett Packard).

Fourier transform IR spectra of Gd-DTPA/DACHPt aqueous complex

Fourier transform IR (FT-IR) spectra were obtained using a FT-IR spectrophotometer (FT/IR 615, JASCO Corp.) with a resolution of 4 cm^{-1}. To characterize the interaction between Gd-DTPA and DACHPt, freeze-dried Gd-DTPA/DACHPt complex at 1:1, 1:5, and 1:10 mixing ratios was milled with KBr and then pressed into a disc for analysis.

Arsenazo III colorimetric assay

The absence of Gd^{3+} in the Gd-DTPA/DACHPt mixture was confirmed by using the arsenazo III method (29). Briefly, Gd-DTPA and DACHPt were mixed at 1:1 molar ratio (0.2 mmol/L) in water. Then, 0.5 mL of this solution was mixed with 0.5 mL of arsenazo III (0.2 mmol/L; Sigma-Aldrich). The absorbance spectra were measured with a spectrometer (V-570 UV/VIS/NIR Spectrophotometer, JASCO). A calibration curve was obtained by measuring the absorbance at 660 nm of a series of standard solutions of the arsenazo III/Gd^{3+} complex prepared by mixing solutions of $GdCl_3$ (Sigma-Aldrich) and arsenazo III in water. The pH of the solutions was maintained at 6.5.

Release rate of DACHPt and Gd-DTPA from the Gd-DTPA/DACHPt–loaded micelles

The release of DACHPt and Gd-DTPA complexes from the micelles was studied by the dialysis method. One milliliter of Gd-DTPA/DACHPt–loaded micelles solution was introduced in a dialysis bag (MWCO: 6,000) and incubated in 99 mL micelles in physiologic conditions (i.e., 10 mmol/L PBS plus 150 mmol/L NaCl at 37°C). The solution outside the dialysis bag was sampled at defined periods. The concentration of Pt and Gd was measured by ICP-MS. The UV-Vis spectra of Gd-DTPA, $GdCl_3$, and the solution outside the dialysis bag were recorded from 270 nm to 280 nm with a UV-Vis spectrometer (V-570 UV/VIS/NIR Spectrophotometer).

Kinetic stability of Gd-DTPA/DACHPt–loaded micelles

The stability of the Gd-DTPA/DACHPt–loaded micelles in physiologic conditions was determined by DLS and static light scattering using a Zetasizer Nano ZS90. The changes in the light scattering intensity were measured at defined time periods. In this analysis, a decrease in the light scattering intensity was associated with a decrease in the apparent molecular weight of the micelles and drug density inside the micelle core as well as in the micelle concentration. The size distribution of the Gd-DTPA/DACHPt–loaded micelles was simultaneously monitored.

Characterization of the r_1 relaxivities

The MR contrast effect of the magnetic nanoparticles was examined by measuring their proton longitudinal relaxivities, r_1, of which the definition is the slope of the concentration dependence given as $1/T_1 = 1/T_{10} + r_1[\mathrm{Gd}]$, where T_1 is the longitudinal relaxation time, $1/T_1$ is the longitudinal relaxation rate contrast in the presence of a paramagnetic species, and $1/T_{10}$ is the longitudinal relaxation rate contrast in the absence of a paramagnetic species. The T_1 of Gd-DTPA/DACHPt–loaded micelles, Gd-DTPA, or Gd-DTPA/DACHPt solution at 0.1, 0.2, 0.3, 0.4, and 0.5 mmol/L was measured at 37°C in water with a 0.59-T ^{1}H-NMR analyzer (JNM-MU25A, JEOL) with a standard inversion-recovery pulse sequence.

Cancer models

CDF_1 mice (female, 6 weeks old) were inoculated s.c. with C-26 cells (1×10^6/mL) and used for biodistribution study, antitumor activity assay, and MRI. BALB/c nude mice (female, 6 weeks old) were inoculated in the pancreas with BxPC3 cells for biodistribution study, antitumor activity assay, and MRI. For the latter model, the mice were anesthetized by isoflurane inhalation, and the pancreas was exposed and injected subserosally with 0.1 mL of BxPC3 cells (5×10^6/mL).

Biodistribution

Biodistribution studies were carried out on C-26 tumor–bearing mice at 10 days after implantation when the mean tumor volume was ~100 mm^3. Oxaliplatin, Gd-DTPA, or Gd-DTPA/DACHPt–loaded micelles were i.v. injected to mice at a dose of 100 μg per mouse on a Pt basis or 100 μg per mouse on a Gd basis. The mice were sacrificed after defined time periods (1, 4, 8, and 24 hours). Tumors, livers, kidneys, and spleens were excised. Blood was collected from the inferior vena cava, heparinized, and centrifuged to obtain the plasma. The samples were dissolved in HNO_3 and evaporated to dryness. The Pt and Gd concentrations were then measured by ICP-MS after the samples were redissolved in 5 N HCl.

***In vivo* MRI of Gd-DTPA/DACHPt–loaded micelles**

MR images were obtained using a 4.7-T UNITY INOVA imaging spectrometer (Varian, Inc.) equipped with a birdcage-type RF coil, 66 mm in diameter. For the T1W of the mice, the following parameters were adopted: spin-echo method, repetition time (TR) = 500 ms, echo time (TE) = 15 ms, field of view (FOV) = 32 × 32 mm^2, matrix size = 256 × 256, and slice thickness = 2 mm. MR images were obtained from C-26 tumor– and BxPC3 tumor–bearing mice when the mean tumor volume was 100 and 400 mm^3, respectively. For all of the mice, transaxial T1W images were taken before injecting Gd-DTPA/DACHPt–loaded micelles as a control. The mice were anesthetized with 1.2% isoflurane during the MRI experiments. The mice were injected i.v. with 5 μmol/kg of Gd-DTPA alone or Gd-DTPA/DACHPt–loaded micelles. The transaxial T1W images were taken with a phantom containing water as a reference signal every 10 minutes for 4 hours. The images were analyzed using Mathematica (Wolfram Research, Inc.) and Excel (Microsoft, Inc.). For each time point, the same level of slices that included the center of the tumors was chosen and segmented by drawing a square that included the tumor area. The pixel intensities in the tissues were compared with the precontrast images and the phantom.

Assessment of therapeutic effect by MRI

MR images were obtained using a 7.0-T MRI scanner (magnet: Kobelco and Jastec; console: Bruker Biospin) with a birdcage-type RF coil, 35 mm in diameter (Rapid Biomedical). The experiment was carried out on BxPC3 tumor–bearing mice at 10 days after implantation when the average size of the tumor was ~60 mm^3. Mice (n = 2) were initially anesthetized with 3.0% isoflurane, orally intubated, and then ventilated with 2.0% isoflurane (Abbott Japan) and 1:2 O_2/room air gas mixture using a rodent ventilator (MRI-1, CWE, Inc.). During MRI scanning, rectal temperature was continuously monitored and maintained at 37.0 ± 0.5°C using a heating pad throughout all scans. T1W MRIs were obtained before and 2 hours after administration of the Gd-DTPA/DACHPt–loaded micelles. The Gd-DTPA/DACHPt–loaded micelles were injected i.v. at 8 mg/kg on a Pt base and 3 mg/kg on a Gd-DTPA base. The control mice were injected i.v. with 30 mg/kg of Gd-DTPA, and they were imaged before and 30 minutes after the injection. The drugs were injected on days 0, 4, 8, 11, and 18. T1W multislice two-dimensional spin echo MRI with fat suppression preparation was obtained with the following parameters: TR = 600 ms (respiratory gating of 100 rpm), TE = 9.5 ms, FOV = 32 × 32 mm^2, matrix size = 256 × 256, slice thickness = 1 mm, and average = 4. Slice orientation of the T1W was transaxial (18 slices, nongap) and horizontal (14 slice, nongap).

Image reconstruction and analysis were performed using ParaVision (version 4.0; Bruker Biospin) and ImageJ (version 1.43; NIH). Regions of interest were identified using a mouse atlas of anatomy, and the volume of the tumors was estimated by the following equation: $V = a \times b^2/2$, where a and b are the major and minor axes of the orthotopic tumors measured from the MR images.

Histology and immunohistochemistry

The excised samples were directly frozen in liquid N_2 for immunohistochemistry or fixed in 4% paraformaldehyde and then paraffin embedded to prepare them for H&E staining. Frozen samples were sectioned at 16-μm thickness in a cryostat, fixed in acetone, and incubated with protein blocking solution (Blocking One Buffer, Nakalai Tesque, Inc.), PECAM-1 (BD Pharmingen), Alexa Fluor 488 secondary antibody (Invitrogen Molecular Probes), and Hoechst (Sigma-Aldrich). The samples were observed by using a Zeiss LSM510 Meta confocal microscope for immunohistochemistry and an Olympus AX80 microscope for H&E staining.

Micro-synchrotron radiation X-ray fluorescence spectrometry analysis

Mice bearing BxPC3 orthotopic tumors were injected i.v. with doses of 3 mg/kg (on a Pt base) of Gd-DTPA/DACHPt–loaded micelles. Four hours after the injection, the mice were

sacrificed and the tumors were excised, frozen in liquid N_2, sliced at 16 μm using a cryostat, and fixed on a polypropylene sheet. Micro-synchrotron radiation X-ray fluorescence spectrometry (μ-SR-XRF) was performed using beamline 37XU (30) at SPring-8, operated at 8 GeV and ~100 mA. The tissue samples were irradiated with incident X-rays with an energy of 14 keV, a beam spot size of 1.3 × 1.3 μm^2, and an intensity of 10^{12} photons/s. The fluorescence X-rays were measured using a Si solid-state detector in air at room temperature. Each sample was mounted on an *x-y* translation stage. The fluorescence X-ray intensity was normalized by the incident X-ray intensity, I_0, to produce a two-dimensional elemental map.

Results

Characterization of Gd-DTPA/DACHPt–loaded micelles

The core-shell micellar nanocarriers with PEG palisade were prepared by preincubating Gd-DTPA and DACHPt at a 1:1 molar ratio for >10 hours in water and mixing this solution with PEG-*b*-P(Glu) (Fig. 1). The incubation of DACHPt with Gd-DTPA may lead to the formation of carboxylato complexes between DACHPt and the carboxylic groups in the DTPA chelator of Gd-DTPA. Accordingly, the FT-IR spectra of the DACHPt, Gd-DTPA, and Gd-DTPA/DACHPt mixtures incubated for 24 hours (Fig. 2A) indicated the appearance of a peak at 1,650 cm^{-1} in the spectra of the Gd-DTPA/DACHPt mixtures assigned to the Pt-COO coordination bond. Moreover, the optimal mixing ratio and incubation time of Gd-DTPA and DACHPt were determined by relaxivity titration. The r_1 of the Gd-DTPA/DACHPt complexes gradually increased up to 4.6 $mmol/L^{-1}s^{-1}$ at a 1:1 ratio from the initial 3.4 $mmol/L^{-1}s^{-1}$ of Gd-DTPA alone (Supplementary Fig. S1A). At DACHPt/Gd-DTPA ratios higher than 1, the r_1 remained constant. In addition, the r_1 of the Gd-DTPA/DACHPt complex gradually increased until 10 hours after mixing. Moreover, the activated state of DACHPt was found to be necessary for binding to Gd-DTPA because the Gd-DTPA/oxaliplatin mixture revealed no increase in the relaxivity (Supplementary Fig. S1B). During the Gd-DTPA/DACHPt complex formation, the stability of the Gd-DTPA complex was evaluated by using the arsenazo III method (29). Consequently, the absence of Gd^{3+}

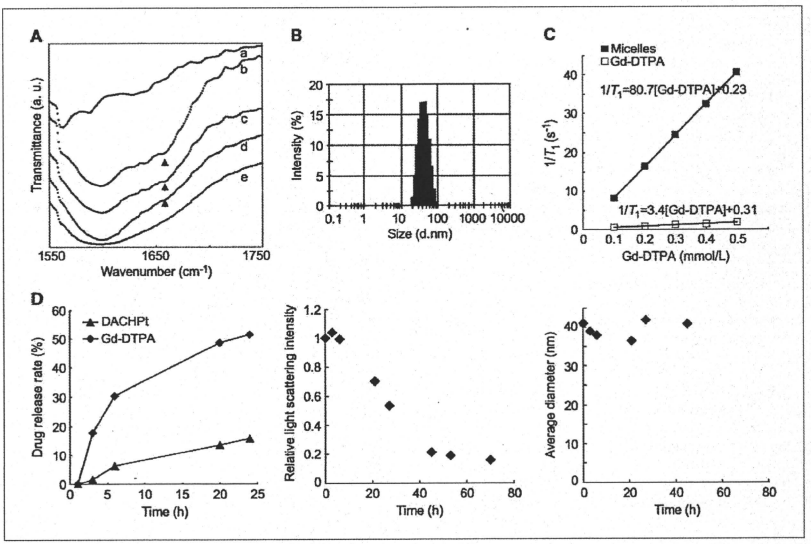

Figure 2. Formation and physicochemical characteristics of Gd-DTPA/DACHPt–loaded micelles. A, FT-IR spectra of DACHPt (a); Gd-DTPA/DACHPt complexes 1:1 (b), 5:1 (c), and 10:1 (d); and Gd-DTPA (e). B, diameter of the micelles determined by DLS. C, longitudinal relaxation ($1/T_1$) of micelles and Gd-DTPA at 37°C. The longitudinal relaxivities (r_1) were calculated from the slope. D, left, release rate of Pt and Gd complexes from Gd-DTPA/DACHPt–loaded micelles in physiologic conditions; middle, relative light scattering intensity of the Gd-DTPA/DACHPt–loaded micelles in physiologic conditions; right, diameter of Gd-DTPA/DACHPt–loaded micelles in physiologic conditions.

in the Gd-DTPA/DACHPt mixture was confirmed (Supplementary Fig. S2).

The obtained micelles were 33 nm in diameter with a narrow size distribution (polydispersity index = 0.067; Fig. 2B). This diameter might be small enough for the micelles to avoid recognition by the reticuloendothelial system, pass through the leaky vasculature of solid tumors by the EPR effect, and attain deep tumor penetration (17). The amounts of DACHPt and Gd-DTPA incorporated in the micelles were found to be 0.42 mg DACHPt/mg polymer and 0.04 mg Gd-DTPA/mg polymer, corresponding to 45% and 5% of the carboxylic groups in PEG-*b*-P(Glu), respectively. Moreover, the r_1 of the micelles increased up to 80.7 mmol/$L^{-1}s^{-1}$, that is, ~24-fold greater than Gd-DTPA alone (Fig. 2C).

The Gd-DTPA/DACHPt–loaded micelles did not release their contents in distilled water (data not shown). However, under physiologic conditions (i.e., 10 mmol/L PBS at 37°C), DACHPt and Gd-DTPA were released in a sustained manner (Fig. 2D, left). Moreover, the release of Gd-DTPA was considerably faster than that of DACHPt, probably due to stronger binding between polymer and DACHPt than between DACHPt and Gd-DTPA. In addition, the safe Gd-DTPA chelates in this system might remain stable because no free Gd^{3+} was detected in the released sample (Supplementary Fig. S3). The gradual drug release from Gd-DTPA/DACHPt–loaded micelles led to a reduction in the light scattering intensity of the micelles (Fig. 2D, middle) due to the decreased density of the micellar cores. Accordingly, the light scattering intensity of the Gd-DTPA/DACHPt–loaded micelles under physiologic conditions decreased to 20% in ~60 hours (Fig. 2D, middle); however, the hydrodynamic diameter of the micelles was maintained at ~30 nm for >48 hours (Fig. 2D, right). The high stability of the micelles and preservation of their hydrodynamic diameter are advantageous in the *in vivo* situation because the structural stability of micelles is highly associated with their prolonged blood circulation (11).

In vivo performance of Gd-DTPA/DACHPt–loaded micelles

The Gd-DTPA/DACHPt–loaded micelles extended the circulation of their cargo in the bloodstream, attaining ~20% of the injected dose of DACHPt after 24 hours and >8% of the injected dose of Gd-DTPA after 4 hours, whereas free oxaliplatin and free Gd-DTPA were rapidly cleared from plasma (Fig. 3A). Moreover, the micelles delivered the drugs to solid tumors due to the increased accumulation and retention at the cancer site because of the EPR effect. Accordingly, the micelles augmented the tumor accumulation 27.7 times for the Pt drug at 24 hours, and >100 times for Gd-DTPA at 4 hours, in subcutaneous murine colon adenocarcinoma 26 (C-26) tumors (Fig. 3B) compared with oxaliplatin and free Gd-DTPA, resulting in high MRI contrast enhancement of the tumor tissue (Fig. 3C). From the ratio of the signal intensities of tumor to muscle, the micelles showed to increase the contrast, whereas the enhancement for Gd-DTPA was almost unchanged. Moreover, the elevated tumor accumulation of Gd-DTPA/DACHPt–loaded micelles may also improve the antitumor activity of the incorporated Pt drug because DACHPt complexes can exert their cytotoxicity after being released from the Gd-DTPA/DACHPt–loaded micelles, as observed in *in vitro* studies (Supplementary Table S1). Accordingly, the micelles showed strong antitumor effect against the C-26 tumor model (Supplementary Fig. S4). Thus, we tested the potential of Gd-DTPA–loaded micelles for monitoring the drug distribution, tumor imaging, and treatment in a pancreatic tumor model close to the clinical situation (i.e., orthotopically inoculated BxPC3 human pancreatic ductal adenocarcinoma tumor).

Direct detection and treatment of pancreatic cancer

The T1W T_1-weighted MR images after i.v. administration of the Gd-DTPA/DACHPt–loaded micelles clearly showed specific contrast enhancement at the tumor area for >4 hours (Fig. 4A and B). In contrast, we did not observe any enhancement in the tumor region after the administration of free Gd-DTPA (Fig. 4A and B), and the signal intensity was higher in the liver, kidney, or spleen than in tumor as suggested from the tumor-to-organ ratios of the MR intensity (Supplementary Table S2). Also, the signals in all organs decreased after 1 hour. The macroscopic observation of the orthotopic tumor-bearing mice that received Gd-DTPA/DACHPt–loaded micelles confirmed the position of every organ and the tumor (Fig. 4D, left and middle), whereas the histologic study of the malignancy revealed the poorly differentiated histology of pancreatic adenocarcinoma, with thick fibrosis and low vascularization (Fig. 4D, right). The amount of Gd-DTPA delivered by the micelles in the orthotopic pancreatic tumor was seven times higher than the accumulation of free Gd-DTPA (Fig. 4C). Accordingly, 3.5% of the total Gd dose from the micelles and 7.2% of the total Pt dose had accumulated within 4 hours of administration.

The antitumor activity of Gd-DTPA/DACHPt–loaded micelles was also evaluated by MRI. Thus, the mice treated with the micelles at 8 mg/kg on a Pt base achieved a significant reduction in the volume of orthotopic BxPC3 tumors (Fig. 5A). Likewise, the weight of the pancreas at day 18 of the micelle-treated animal was much lower than the mice that received only Gd-DTPA (Fig. 5B). Moreover, Gd-DTPA/DACHPt–loaded micelles were shown to enhance the signal intensity at the tumor region (Fig. 5C). Thus, Gd-DTPA/DACHPt–loaded micelle can be used to follow the micelle accumulation in the tumor and the tumor size by MRI, supporting the theranostic concept.

The microdistribution of the drugs at the tumor site was studied using μ-SR-XRF on the pancreatic lesions. Besides the elements traditionally present in animal tissue, such as S, Cl, K, Ca, Fe, Cu, Ni, and Zn, very distinct Pt-L and Gd-L peaks can also be observed in the sum spectrum of the line scan. Thus, the distribution of several atoms (Fe, K, Gd, and Pt) in the tissue sections of the whole pancreas was studied to evaluate the tissue properties and layout of the drugs. The elemental mapping of Fe presents areas with high concentration probably involving the vicinity of blood vessels and the